Response of extreme rainfall to atmospheric warming and wetting: implications for hydrologic designs under a changing climate

Jinghan Zhang [1,2], Long Yang [1,2*], Miao Yu [3], Xiaodong Chen [4]

[1] School of Geography and Ocean Science, Nanjing University, Nanjing, China
[2] Frontiers Science Center for Critical Earth Material Cycling, Nanjing University, Nanjing, China
[3] Chinese Academy of Meteorological Sciences, Beijing, China
[4] Atmospheric Sciences and Global Change Division, Pacific Northwest National Laboratory, Richland, Washington, USA

*Correspondence to: L. Yang (yanglong@nju.edu.cn)

Manuscript for *Journal of Geophysical Research: Atmospheres*
22 December 2022

Key points

- We discern response of extreme rainfall to individual impact of atmospheric warming and atmospheric wetting.
- Dynamic feedbacks from the thermodynamic changes dictate the non-monotonic rainfall response to either warming or wetting.
- The non-monotonic rainfall response is more clearly revealed at fine spatial scales rather than over the entire model domain.

Abstract

Understanding the processes of rainfall extremes and their response to anthropogenic climate change is pivotal for improved adaptation of unprecedented flood hazards around the world. Here we take the record-breaking 20 July 2021 storm over central China, characterizing the upper tail of rainfall intensity spectrum over mainland China, as an example. We investigate the response of this particular storm to atmospheric warming (i.e., increase in air temperature) and wetting (i.e., increase in atmospheric moisture content) based on a series of convection-permitting model simulations. Our results show non-monotonic changes of the space-time rainfall variability to either increased temperature or atmospheric moisture content. The non-monotonic rainfall response is more clearly revealed at fine spatial (100-1000 km^2) and temporal scales (less than 6 hours) rather than over the entire domain (10^4 km^2) and aggregated over the storm duration (around two days). This is mainly attributable to the distinct feedbacks from atmospheric dynamics (i.e., moisture convergence and interaction with regional topography) rather than regulated by thermodynamic changes alone. Atmospheric warming poses notable changes in the vertical structure of storm cells, contributing to reduced areal reduction factors at small spatial scales and short durations, while atmospheric wetting additionally modifies storm evolution properties. Our modeling analyses challenge the existing practices for hydrologic designs under a changing climate, highlighting particular vulnerability for cities or small basins to short-duration rainfall extremes and the resultant flash flood hazards.

Plain Language Summary

Understanding rainfall extremes and their response to climate change plays a pivotal role in improved hydrologic designs and flood adaptation strategies. In this study, the 20 July 2021 storm that produced record-breaking rainfall over central China is used to examine the response of rainfall extreme to atmospheric warming and wetting (i.e., increase in air temperature and atmospheric moisture content, respectively) through a series of high-resolution model simulations. Our results find that the coverage of heavy rainfall and peak rain rate show non-monotonic changes with either atmospheric warming or wetting. It is tied to modified atmospheric dynamics in the changing storm environment. Insights into rainfall processes at finer spatial scales and shorter durations reveal more details about the factors that dictate the non-monotonic responses. We imply that it is not safe to adopt conventional practices in hydrologic designs, including the estimation of probably maximum precipitation, areal reduction factors for hypothetical extreme storms (or design storms). We also highlight the great sensitivities of short-duration rainfall extremes due to changes in either temperature or moisture content. This would pose great challenges to the safe design for cities or small basins that are particularly vulnerable to these types of hydrological extremes.

1 Introduction

Central China experienced catastrophic extreme rainfall and flooding during 19-20 July 2021 (referred to as the 20 July 2021 storm below), leaving 398 fatalities and more than 14 million people affected. The maximum hourly rainfall of 201.9 mm set the new record over mainland China, with additional 19 rain gauges breaking the daily records since gauge establishment. There are 21 rain gauges with 48-hour rainfall accumulation exceeding 600 mm, comparable to the annual rainfall totals. The 20 July 2021 storm is neighbored by another two "poster-child" storms that broke multiple rainfall records over China, including the maximum 6-hour rainfall accumulation of 830.1 mm (also the world rainfall record) from the August 1975 storm (Yang et al., 2017) and the maximum 7-day rainfall accumulation of 2,050 mm from the August 1963 storm (Yang et al., 2021). The 20 July 2021 storm, the August 1975 storm, and the August 1963 storm over central China define the upper tail of rainfall intensity spectrum over mainland China, and are also responsible for several record floods in the world (Yang et al., 2017). Understanding physical processes of these rainfall extremes and their responses to anthropogenic climate change plays a critical role in developing improved adaptation and mitigation strategies for unprecedented flood hazards (IPCC, 2021; Kreibich et al., 2022; Pendergrass, 2018).

Increase in global mean temperature (i.e., atmospheric warming) is the most certain facet of anthropogenic climate change (IPCC, 2021). The impact of atmospheric warming on rainfall changes can be approximately regulated by the Clausius-Clapeyron (C-C) equation, with rainfall intensities increased by 7 % per Celsius degree due to the increased water-holding capacity in the atmosphere (Allan & Soden, 2008; Allen & Ingram, 2002; O'Gorman & Schneider, 2009; Trenberth et al., 2003). The response of extreme rainfall to atmospheric warming can deviate far beyond the C-C scaling rate (Pendergrass, 2018; Pfahl et al., 2017). This is evidenced by both empirical analyses (Lochbihler et al., 2017; Papalexiou & Montanari, 2019; Utsumi et al., 2011; Wasko & Sharma, 2015; Wasko et al., 2016) and numerical experiments (Asadieh & Krakauer, 2015; Guo et al., 2016; Huang et al., 2020; Nie et al., 2020; Pfahl et al., 2017). The super CC scaling highlights the important role of associated changes in atmospheric circulation (e.g., moist convergence) and atmospheric instability (updraft, e.g., Pendergrass, 2018), in addition to increased lower-tropospheric water vapor (e.g., Held & Soden, 2006; Kim et al., 2022), in dictating extreme rainfall response to atmospheric warming. However, it remains less elucidated about the direct impact of changes in atmospheric moisture content alone, i.e., atmospheric wetting, on rainfall extremes.

Understanding the impact of atmospheric wetting on rainfall extremes is also motivated by reliable estimates of Probable Maximum Precipitation (PMP) under a changing climate. PMP is defined as the largest rainfall depth for a given duration meteorologically possible for a particular location (World Meteorological Organization, 2009). It serves as the basis for the engineering community in flood-control infrastructures designs. The conventional PMP estimation approach assumes a linear relationship between rainfall depth and atmospheric moisture content (Abbs, 1999). The maximum rainfall depth, i.e., PMP, can be obtained through maximizing a historical storm by multiplying the ratio of climatologically maximum precipitable water (estimated from dew point temperature) to the precipitable water when the historical storm is observed (e.g., Chen & Hossain, 2019; Salas et al., 2020). However, this linear assumption has been challenged by previous studies relying on numerical models for PMP estimation (Ohara et al., 2017; Yang & Smith, 2018; Zhao et al., 1997). For instance, Yang and Smith (2018) show notable reduction of rain rates at various spatial and temporal scales when the storm environment is close to saturation. Their analyses highlight the dictation of rainfall response to atmospheric moisture content by small-scale convective activities as well as the role of orographic lifting. The conventional PMP estimation approach additionally assumes a constant precipitation efficiency, representing how efficient precipitation is produced from convective systems (e.g., Sui et al., 2007), when the storm environment becomes saturated. Since precipitation efficiency is intricately dictated by atmospheric dynamics at regional (e.g., convergence, environmental wind shear) and local scales (e.g., updraft, Breugem et al., 2020), the validity of this constant assumption remains largely unknown.

Previous studies paid more attention on how to create a “worst-case” scenario for PMP estimates, but less on the responses of the simulated atmospheric fields to water vapor content and their drivers. There are extensive efforts in numerical-model based PMP estimation approaches, including increasing moisture profiles (Ishida et al., 2015b; Odemark et al., 2021), atmospheric boundary condition shifting (Ishida et al., 2015a; Ohara et al., 2011; Toride et al., 2019), or different combinations of existing methods (Hiraga et al., 2021; Ishida et al., 2018). Quantifying the factors (e.g., convergence, moisture transport, storm structure and evolution) that dictate the rainfall response to atmospheric wetting can provide improved understandings on the changes of rainfall extremes under future climates (e.g., Kunkel et al., 2020).

In this study, we examine the individual impact of atmospheric wetting (i.e., increase in atmospheric moisture content) and warming (i.e., increase in air temperature) on extreme rainfall. We take the 20 July 2021 storm over central China as the test case, primarily due to its extremeness and the abundance of observational records. The goal is to reveal the full spectrum of rainfall responses to atmospheric wetting and warming by gradually increasing atmospheric moisture content and air temperature. We identify the physical processes that are responsible for contrasting rainfall responses to those thermodynamic changes. These aims are pursued based on the Weather Research and Forecasting model (WRF) simulations under different moisture-perturbation and temperature-perturbation scenarios for the storm, while maintaining the large-scale atmospheric circulation unchanged (see section 2 for details).

Unlike previous studies that mostly rely on global or regional climate models with coarse spatial resolutions (~10 km or beyond, Afzali-Gorouh et al., 2022; Beauchamp et al., 2013; Kunkel et al., 2013) or focus on long-duration rainfall extremes (daily scale or beyond, e.g., Gangrade et al., 2018; Hiraga et al., 2021), our convection-permitting WRF simulations with the spatial resolution of 1 km allow us to examine rainfall structures at fine spatial scales (e.g., less than 100 km^2) along with short durations (e.g., sub-hourly and hourly). Empirical analyses show substantially faster intensification of sub-hourly rainfall extremes than those at sub-daily scales (Ayat et al., 2022), implying the scale-dependence of rainfall response to anthropogenic climate change (Fowler et al., 2021). We expect to provide additional modeling insights by examining rainfall structures at multiple spatial and temporal scales. These analyses are used to inform improved hydrologic designs (including estimation of areal rainfall for hypothetic extreme storms or design storms, PMP estimates) under a changing climate, especially for cities or small basins that are vulnerable to short-duration rainfall extremes and the resultant flash flood hazards.

2. Data and Methodology

2.1 In-situ rainfall observations

We examine extreme rainfall from the 20 July 2021 storm based on a dense network of rain gauges over Henan province, central China. There are 2265 rain gauges in total (Fig. 1), with hourly rainfall observations during the entire storm period, i.e., 00 UTC 17 July-23 UTC 22 July, 2021. The dataset is provided by the Chinese Meteorological Agency, and has been through strict quality control procedures (see e.g., Yu et al., 2007 for details).

2.2 WRF simulations

The WRF model is a fully compressible, non-hydrostatic, mesoscale model (Skamarock et al., 2021). The Advanced Research version of WRF (version 3.9.1) is used in this study. We configure three one-way nested domains (Fig. 1). The horizontal grids are 380×350, 370×343, 352×331, with horizontal grid spacing of 9 km, 3 km, and 1 km, respectively. We set 38 sigma levels, with the echo top set at 100 hPa. The other physics options are the Yonsei University (YSU) boundary layer scheme, the Rapid Radiative Transfer Model (RRTM) for longwave radiation, the Dudhia's scheme for shortwave radiation and the Noah land surface model coupled with the single layer urban canopy model to capture heat, moisture and momentum exchange below land surfaces and the lower atmosphere. We use the JRA-55 reanalysis fields for the model's initial and boundary conditions. The spatial and temporal resolution of the JRA-55 reanalysis fields is 1.25-degree by 1.25-degree and 6-hour, respectively. Since the choice of microphysics schemes plays an important role in rainfall simulation (Chawla et al., 2018; Mohan et al., 2018; Rajeevan et al., 2010; Tewari et al., 2022), we carry out test runs by choosing different microphysics schemes, while maintaining other physics options unchanged. The microphysics schemes being tested include the Thompson scheme, the Morrison double-moment scheme, and the WRF 6-class single-moment scheme. We ultimately choose the Thompson scheme, since the simulated rainfall with this microphysics scheme best agrees with the rain gauge observations (results not shown).

The WRF simulation with aforementioned configurations is referred to as the control simulation (i.e., CTRL). We conduct additional WRF simulations to examine the response of spatial and temporal rainfall variability from the 20 July 2021 storm to separated changes in atmospheric moisture content and air temperature. We increase the atmospheric moisture content by modifying the relative humidity field at all atmospheric levels. The modification are implemented for both initial and boundary conditions by following the equation below (similarly also see Yang & Smith, 2018):

$$RH = \alpha(100 - RH_0) + RH_0 \tag{1}$$

where RH_0 represents the relative humidity (in %) in the reanalysis fields, while RH represents the relative humidity (in %) after moisture adjustment. The multiplication parameter α varies from 0.1 to 1.0 with an interval of 0.1. This generates ten WRF simulations in total (i.e., moisture-perturbation scenarios). Inter-comparisons of these simulations allow us to examine rainfall responses to the gradual increases in atmospheric moisture content. The ten WRF simulations are referred to as RH10 (α=0.1), RH20 (α=0.2), …, RH90 (α=0.9), and RH100 (α=1.0). The RH100 simulation, with the atmosphere completely saturated, imitates the storm environment for PMP as prescribed by the conventional PMP estimation approach.

Similarly, we examine rainfall response to changes in air temperature. We uniformly increase the air temperature field for both the surface (i.e., at 2 meters) and all atmospheric levels by 1 °C, 2 °C and 3 °C, respectively. The WRF simulations with different temperature increments (i.e., temperature-perturbation scenarios) are referred to as AirT1 (ΔT=1 °C), AirT2 (ΔT=2 °C), and AirT3 (ΔT=3 °C), respectively. We note that for temperature changes, the relative humidity field is maintained the same as the CTRL simulation. Since the saturated water vapor pressure (representing the water-holding capacity) is monotonically associated with air temperature, we thus expect increases in precipitable water integrated within the entire atmospheric column when air temperature is increased. This is also known as the Pseudo-global warming scenario, and is frequently adopted in climate attribution analyses (e.g., Schar et al., 1996). Here we assume a uniform increase of air temperature at all atmospheric levels. This enables us to focus on rainfall response to absolute temperature changes rather than addressing the impact of uneven warming rates at different levels (similarly see Kreienkamp et al., 2021; Yang et al., 2021).

Table 1 provides an overview of different WRF simulations implemented in our study. All the simulations are initiated at 00 UTC 19 July, and run for 48 hours. The first six hours are regarded as the spin-up period, and are not included in the following analyses. The integral time step is 18 s for the outer domain, and is 2 s for the innermost domain. We mainly focus on the innermost domain due to its high spatial resolution to resolve fine-scale convective activities (e.g., Ban et al., 2014; Prein et al., 2015; Weisman et al., 1997).

2.3 Storm tracking

We examine the structure and evolution properties of the storm as well as their responses in different moisture and temperature conditions based on the Thunderstorm Identification, Tracking, Analysis, and Nowcasting (TITAN) algorithms (Dixon & Wiener, 1993). The TITAN algorithms rely on the simulated reflectivity fields from the innermost domain of the WRF simulations. Storm tracking analyses enable us to examine the responses of sub-hourly rainfall extremes under different moisture and temperature-perturbation scenarios. This is because although the model output is at 1-hour interval, the simulated reflectivity field represent the instantaneous characterization (or snapshot) of the storm system. We define a storm cell if the volume of a spatially contiguous region exceeds 5 km^3 with the simulated reflectivity of each grid within the region larger than 45 dBZ (similarly also see e.g., Yang & Smith, 2018). Our results are not sensitive to different sets of thresholds used in the tracking algorithms.

3. Synoptic environment of the 20 July 2021 storm

The 20 July 2021 storm demonstrate a combination of favorable ingredients for extreme rainfall (Liang et al., 2022; Yin et al., 2022). An important synoptic feature that is directly responsible for the record-breaking rainfall is the remote moisture transport from Typhoon In-fa (2021) (Yu et al., 2022). Typhoon In-fa (2021) is initiated over west-northwest of Guam, and moves towards the Philippine Seas after its initiation. It becomes a mature tropical cyclone on 18 UTC July 19 (Fig. 2a). The Western Pacific Subtropical High (WPSH, represented by the contour of 5880 gpm at 500 hPa) is located over the Sea of Japan. On 06 UTC July 20, the WPSH is strengthened and extended westwards over the East Asian continent. The increased pressure gradient between WPSH and Typhoon In-fa (2021) facilitates the establishment of a zonal pathway for strong moisture transport in the form of low level jets from the East China sea towards central China (Fig. 2b). The wind speed at 700 hPa exceeds 20 m s^{-1}. The integrated vapor transport exceeds 500 kg m^{-1} s^{-1}. The westward extension of WPSH further directs the moist plume to impinge onto Mt. Taihang (with the orientation of southwest towards northeast). Convection is enhanced through orographic lifting and topographic blocking. The maximum convective available potential energy (CAPE) is 2940 J kg^{-1} at 06 UTC or 14 LST (i.e., three hours before maximum hourly rainfall), with the spatial extent of CAPE exceeding 1000 J kg^{-1} covering 32,000 km^2. The maximum precipitable water is 70 mm, indicating that the record-breaking rainfall occurs in an extremely moist and unstable environment over central China. Extreme rainfall at small temporal and spatial scales are also closely tied to the spatial organization of mesoscale convective storm cells (Li et al., 2020; Lochbihler et al., 2017; Luo et al., 2014). This involves the impact of regional topography and its interactions with the location of the convergence zones. These combinations of favorable ingredients contribute to the maximum hourly rainfall of 201.9 mm on 09 UTC 20 July (i.e., 17 LST). We refer the readers to Fu et al. (2022) and Yin et al. (2022) for the mesoscale ingredients responsible for the record-breaking rainfall. The storm propagates northwards after producing record-breaking hourly rainfall. This is partially tied to the confluence of a southern moist plume by Typhoon Cempaka (2021). The WPSH is weakened on 18 UTC July 20 (Fig. 2c). On 06 UTC July 21, the contour of 5860 gpm extends southward, and cuts off the moisture transport path from Typhoon In-fa (Fig. 2d). Heavy rainfall quickly ceases due to insufficient supply of moist plume and the injection of dry, cold air from higher latitudes to the north of the Henan province.

A notable feature of the large-scale environment for the storm is that both the subtropical high and Typhoon In-fa (2021) show slow motion during the two-day period. The stable synoptic configurations facilitate persistent moisture supply and repeated convection over a fixed region (Liang et al., 2022). Comparable large-scale circulation pattern was also observed for the 7 August 1975 storm over the upper Huai River basin, central China (Yang et al., 2017; Zhang et al., 2022). The August 1963 storm is associated with remote moisture transport from a typhoon (i.e., Typhoon Besse) over the Eastern China sea, along with the role of regional topography in dictating extreme rainfall (Yang et al., 2021). The three storms, i.e., the 20 July 2021 storm, 7 August 1975 storm, and 8 August 1963 storm, demonstrate comparable synoptic configurations (i.e., easterly moisture transport from the Pacific, northern blocking by continental high-pressure systems) and mesoscale ingredients (i.e., topography, low level jets) for extreme rainfall over central and northern China. The resemblance among these record-breaking rainfall events in recent history highlights the potential of the 20 July 2021 storm as a perfect candidate for PMP estimates over China.

4. Modeling analyses

4.1 Comparison of CTRL simulation against in-situ observations

We evaluate the CTRL simulation in reproducing the 20 July 2021 storm by comparing the simulated rainfall against in-situ rain gage observations. Extreme rainfall mostly occurred within the municipal boundary of Zhengzhou city (see the black box in Fig. 3a), with storm-total rainfall accumulation (that is from 06 UTC 19 July to 00 UTC 21 July) exceeding 600 mm for 18 rain gages.

The observed maximum rainfall accumulation in the 42-hour duration is 833 mm. The CTRL simulation captures the spatial structure of extreme rainfall reasonably well, although there is a slight underestimation in rainfall magnitudes (Fig. 3b). The maximum rainfall accumulation from the model is 654 mm. The location of maximum rainfall is approximately 50 km offset towards west of the observed storm center, but is still within the municipal boundary of Zhengzhou city. A similar spatial offset is also reported in previous simulations for the storm (e.g., Luo et al., 2022; Wang et al., 2022; Xu, Duan, Li, et al., 2022). We compute the equitable threat score (ETS) for the simulated rainfall to get a quantitative evaluation of the model's performance. ETS measures the match of forecast/simulated events to observations with the match due to randomness accounted for. It is widely used in the verification of quantitative precipitation forecasts (Stanski et al., 1989; Wilks, 1995). The ETS score is computed by difference between observations and simulations at all gauge sites and the corresponding model grids, based on a given threshold. The domain averaged ETS is 0.26 (using 150 mm as the rainfall threshold), which is above the commonly used threshold of 0.2 as the indication of good forecasts (e.g., Pennelly et al., 2014; Wang, 2014; Zhang et al., 2019). Our evaluation indicates that CTRL simulation captures the key spatial pattern of storm-total rainfall.

In addition to the spatial pattern, the CTRL simulation captures the main feature of temporal rainfall variability for the storm. There are two rainfall pulses during the 2-day period over the innermost domain. The correlation coefficient between the time series of domain-averaged simulated rainfall and rain gauge observations is 0.59 (P<0.01, based on the Wald Test with t-distribution, same below). The maximum hourly rainfall is observed during the late afternoon (around 16-17 local time or 0800-0900 UTC) on July 20. The CTRL simulation fails to reproduce maximum hourly rain rainfall of 201.9 mm. The mean rainfall intensity (i.e., 8.8 mm/h) over the grids with rain rate exceeding 100 mm/h is close to that of gauge observations (i.e., 13.3 mm/h, Fig. 3d). This indicates that the model is able to reproduce key mesoscale rainfall processes within the innermost domain, even though the fine-scale convection might be under-represented. The simulation bias highlights the challenge of existing convection-permitting models in capturing fine-scale processes of extreme rainfall (Dyrrdal et al., 2018; Patel et al., 2019; Terzago et al., 2018). Improved model performance can be pursued through adopting smaller integral time steps (Yin et al., 2022), finer grid spacing (Kendon et al., 2014; Lucas-Picher et al., 2021; Prein et al., 2013), or large-member ensemble simulations with varying parameterizations or initial/boundary forcings (Wang et al., 2022; Xu, Duan, & Xu, 2022). These efforts are, however, beyond the scope of the present study. The performance of our model configurations is comparable to (if not superior than) previous simulations of the storm based on state-of-art modeling techniques (Luo et al., 2022; Xu, Duan, & Xu, 2022; Zhu et al., 2022). We rely on this model configurations and the corresponding modifications to examine the response of spatial and temporal rainfall structures to the changing thermodynamic fields (i.e., moisture and temperature).

4.2 Moisture-perturbation scenarios

Figure 4 shows the spatial coverage and mean intensity of rainfall from the WRF simulations with contrasting atmospheric moisture contents. A notable feature is that both the mean rain rate over the rainy grids (with rain rate exceeding 0.1 mm h^{-1}, Fig. 4a) and over the heavy rainfall grids (with rain rate exceeding 20 mm h^{-1}, Fig. 4c) show little variations with gradual increases in atmospheric moisture content (i.e., increasing α). This indicates a weak response of domain-scale mean rain rate to the changing atmospheric moisture content for the storm. However, if we focus on the spatial rainfall coverage, the variations among different moisture conditions are significant. The spatial coverage of rainy grids during the entire storm period remains almost constant when the atmosphere is moderately moistened (with α below 0.4, Fig. 4b), while the spatial coverage of heavy rainfall grids shows a slightly increasing tendency (Fig. 4d). Further moistening the atmosphere contributes to notable reductions in the spatial coverages of both the rainy and heavy rainfall grids. For instance, the mean proportion of the rainy grids within the innermost domain is 67 % for the RH40 simulation, and is reduced sharply to 35 % when the atmosphere is saturated (i.e., RH100). The mean spatial coverage of heavy rainfall grids for the RH40 simulation is more than 2.4 times as large as that for the RH100 simulation (Fig. 4d). The parabolic tendency of heavy rainfall coverage changes among different WRF simulations highlight the non-monotonic rainfall responses to atmospheric moisture content.

We choose three members from the ten moisture-perturbation simulations, i.e., RH40, RH70, and RH100, to better reveal the contrasting space-time rainfall structures for the storm under different moisture conditions. Figure 5 shows the spatial distribution of rainfall accumulation from the three WRF simulations as well as their differences with respect to the CTRL simulation (Fig. 2d). There is a weak storm core within the municipal boundary of Zhengzhou for the RH40 simulation, even though the maximum rainfall accumulation (i.e., 654 mm) is comparable to the CTRL simulation (at a different location, Fig. 5a). The weakened storm core is accompanied by increased rainfall accumulation by around 150-250 mm outside Zhengzhou (Fig. 5b). The coverage of reduced rainfall accumulation further expands from Zhengzhou to its surrounding regions when the atmosphere is further moistened (RH70, Fig. 5d). When the atmosphere becomes entirely saturated, i.e., the RH100 simulation, we note that the entire domain is covered by negative rainfall anomalies relative to the CTRL simulation (Fig. 5f).

Changes in the atmospheric moisture content significantly modify the temporal rainfall variability over the domain as well (Fig. 6). The timing and magnitude of domain-averaged rain rate is almost similar between RH40 and the CTRL simulation, while further moistening the atmosphere leads to reduced magnitude and earlier onset of rainfall peak over the domain (Fig. 6a). For the RH100 simulation, the peak rain rate is observed only two hours after the model's initiation. Earlier rainfall onset depletes precipitable water in the atmosphere. This is not favorable for the accumulation of convective available potential energy over the domain. The maximum CAPE is 3422 J kg^{-1} for the RH40 simulation, with 8790 km^2 exceeding 2500 J kg^{-1} (Fig. 7b). The spatial extent of high CAPE is larger for RH40 than the CTRL simulation. This partially explains the increased rainfall outside Zhengzhou in the RH40 simulation (Fig. 5b). The spatial coverage of CAPE exceeding 2500 J kg^{-1} is 5550 km^2 and 136 km^2 for the RH70 and RH100 simulation, respectively (Fig. 7d).

The variability of domain-average rainfall is dictated by the domain-wide water vapor convergence (Fig. 6c), but is less related to the variability of either precipitable water (Fig. 6b) or evaporation (Fig. 6d). For instance, the correlation coefficient between domain-average rain rate and water vapor convergence is 0.82, 0.67, and 0.65 for the RH40, RH70, and RH100 simulation, respectively (P<0.01). The reduced water vapor convergence when the atmosphere is saturated (i.e., the RH100 simulation) is mainly attributed to the weakening of a vortex (known as the Huang-huai Cyclone) to the southwest of the domain. The vortex plays a critical role in relaying moisture transport from Typhoon In-fa (2021) into the storm region. Moistening the atmosphere leads to the weakening of the vortex (as represented by the reduced gradients of the 850 hPa contours). A notable feature is the reduction of wind speeds at 700 hPa when the atmosphere is close to saturation, leading to reduced water vapor transport into the domain, e.g., maximum IVT lower than 500 kg m^{-1} s^{-1} for

RH100 simulation (Fig. 8). Moderately moistening the atmosphere (with α below 0.4) does not show notable impacts on the mesoscale structure of the vortex and the water vapor transport pathway.

The weakening vortex also leads to slight but noticeable changes in the orientation of synoptic inflows. When the atmosphere is approaching saturation, i.e., the RH70 and RH100 simulation, the composite wind at 700 hPa shifts from southeasterly towards more southerly (around 116°, with 0° as the due north). In contrast, the orientation of the composite wind for the CTRL and RH40 simulation is more perpendicular to the regional topography (around 120°). Our analyses highlight the role of the associated changes in the atmospheric dynamics under different moisture conditions in dictating the non-monotonic rainfall changes for the storm.

4.3 Temperature-perturbation scenarios

Figure 9 shows the spatial coverage and mean intensity of domain-wide rainfall from the WRF simulations with different temperature increments. We identify weak variations in mean rain rate either over the rainy grids (with rain rate exceeding 0.1 mm h^{-1}, Fig. 9a) or over the heavy rainfall grids (with rain rate exceeding 20 mm h^{-1}, Fig. 9c) within the inner domain when the air temperature is gradually increased. This is consistent with rainfall response to the changes in atmospheric moisture content at the domain scale (Fig. 4). The small tendency maintains for the coverage of rainy grids as well. However, there is a "hook" structure (i.e., first increase and then decrease) of the changing heavy rainfall extents over the domain (i.e., the mean value of the boxplots, Fig. 9d). The mean extent of heavy rainfall attains its maximum when the air temperature is increased by 2 °C. In addition, both the AirT2 and AirT3 simulation witness increased maximum rainfall accumulation compared to the CTRL simulation, i.e., 761 mm for AirT2 and 697 mm for AirT3. The spatial pattern of rainfall changes is comparable across different warming scenarios (Fig. 10), except that the region of enhanced rainfall is located outside Zhengzhou.

Increases in air temperature does not lead to notable shifts in the temporal variability for either domain-average rain rate or water vapor convergence (Fig. 11). This contrasts to the rainfall response to the changes in atmospheric moisture content as shown in Fig. 6 (where we see an earlier onset of rainfall peak when the atmospheric moisture content is increased). For every 1 °C increase in air temperature, there is approximately 4-5 mm increase of precipitable water in the atmospheric column (Fig. 11b). The comparable domain-average spatial and temporal rainfall variability under different temperature increments (Fig. 10 and Fig. 11) point to the inertia of large-scale atmospheric dynamics to atmospheric warming (e.g., Haerter & Berg, 2009; Molnar et al., 2015). This is further evidenced by the consistent patterns of water vapor fluxes under different warming scenarios (Fig. 12). We identify a small region within domain 3 for the AirT2 simulation that experience most intense water vapor transport (i.e., exceeding 800 kg m^{-1} s^{-1}, Fig. 12c). This is consistent with the "hook" structure of contrasting heavy rainfall extent under different warming scenarios (Fig. 9d). However, we find consistently increased rainfall over domain 2 (with the grid spacing of 3 km, figure not shown). The mean rainfall intensity over domain 2 is increased by 7.8 % compared to the CTRL simulation for every 1 °C increment in air temperature. This aligns with the Clausius-Clapeyron rate of ~7 % K^{-1} (e.g., Pall et al., 2007). The contrasting rainfall response at different spatial and temporal scales highlight the necessity of further examining rainfall processes at finer spatial scales and shorter durations. Fine-scale characterizations of rainfall structures can provide additional insights into the non-monotonic rainfall response to changes in either atmospheric moisture content or air temperature.

5. Implications for hydrologic designs under a changing climate

5.1 Depth-area-duration curves

We examine the depth-area-duration (DAD) curves for the 20 July 2021 storm to highlight rainfall structures at fine scales and under different scenarios. The DAD curves provide critical references for developing areal mean rainfall of hypothetical extreme storms (or design storms) in flood-control infrastructures designs (e.g., Dhar & Nandargi, 1993; Rastogi et al., 2017; Svensson & Rakhecha, 1998). To derive the DAD curves, we first identify the maximum *X*-hour domain-average rainfall using moving windows of the corresponding hours (*X* equals to 3, 6, and 12). We select the grid with maximum *X*-hour rainfall depth, and then calculate the maximum of average rainfall depth through gradually expanding the radius of the spatial extent centered on the grid with maximum rainfall depth. The areal reduction factor (ARF), defined as the ratio of maximum rainfall depth averaged over certain spatial extents to the point-scale maximum rainfall depth, can be subsequently derived from the DAD curves. The procedures are repeated for each of the WRF simulations as listed in Table 1.

Figure 13 shows the DAD curves derived for the CTRL simulation and under three moisture-perturbation scenarios, i.e., for the RH40, RH70, and RH100 simulation. Moderately moistening the atmosphere (i.e., the RH40 simulation) increases maximum 3-hour rainfall depth for all spatial scales (Fig. 13a). The increment of maximum 6-hour rainfall depth or the RH40 simulation is not evident for spatial scales smaller than 1000 km^2, but is still notable beyond that (Fig. 13b). Both the RH70 and RH100 simulation show considerable reduction of maximum 3-hour and 6-hour rainfall depth, with the reduction rate larger in small (i.e., less than 1000 km^2) than large spatial scales (Fig. 13a and 13b). The maximum 3-hour rainfall depth is 239 mm averaged over a 100 km^2 area for the RH40 simulation. It is more than twice as large as that for the RH70 (i.e., 122 mm) and RH100 simulation (i.e., 110 mm, Fig. 13a). This is associated with the elevated maximum CAPE, i.e., a moderate increase in moisture providing a more favorable environment for mesoscale convection (Fig. 8b). The maximum 12-hour rainfall depth shows gradual decreases with atmospheric moisture content at all spatial scales (Fig. 13c). This is consistent with Fig. 4d that shows the decreased spatial coverage of heavy rainfall with increased atmospheric moisture content over the entire storm period (i.e., 42 hours). The contrasting DAD curves further highlight the non-monotonic dependence of the rainfall variability on atmospheric moisture content, especially at small spatial scales and short durations.

By contrast, the DAD curves under three temperature-perturbation scenarios show increased rainfall depths at almost all spatial scales when the temperature increment is 2 °C, relative to the CTRL simulation. The increased rainfall depth is only observed at small spatial (less than 100 km^2) scales and short durations (3-hour and 6-hour) when the temperature is increased by 1 °C (Fig. 13). More specifically, the maximum 3-hour rainfall depth at point scale and averaged over 10 km^2 for the AirT1 simulation is 300 mm and 290 mm, the largest of all scenarios. Another notable feature is that the impact of temperature increment (less than 2 °C) on increased rainfall intensity is more significant than the impact of moderately moistening the atmosphere, i.e. the RH40 simulation, especially at small spatial scales (less than 100 km^2) and short durations (3 hours and 6 hours, Fig. 13). This might be associated with the positive feedbacks of atmospheric warming on enhancing local convection through latent heat release (Pendergrass et al., 2019; Prein et al., 2017; Trenberth et al., 2003; Westra et al., 2014). Further warming (i.e., temperature increment equals to 3 °C) leads to reduced rainfall accumulation at all scales. This is probably induced by the decreased duration of precipitation over the domain (Fig. 11a, e.g., Panthou et al., 2014; Utsumi et al., 2011; Wasko et al., 2015). Our results highlight the potential of anthropogenic warming in further increasing the storm's extremeness, and thus needs particular attention for future flood adaptation strategies.

Table 2 lists the ARFs at 100 km^2, 1000 km^2, and 10,000 km^2 under different moisture and temperature-perturbation scenarios. Again, the ARF does not exhibit linear response to either atmospheric moisture content or air temperature perturbations. For instance, the ARFs for the RH40 simulation are larger than or at least equal to those derived from the CTRL simulation at all spatial and temporal scales, while further moistening the atmosphere (i.e., for the RH70 and RH100 simulation) can lead to either increase or decrease of the ARFs depending on the scales of interest. Similar is true for the temperature-perturbation scenarios, except that the ARFs seem to progressively decrease for the 3-hour and 6-hour durations and over 100 km^2. This indicates that the peak rain intensity increases more sharply than the average rain rate over the 100 km^2 under atmospheric warming.

5.2 Structure and evolution properties of storm cells

We look into rainfall structures at sub-hourly scale through examining the structure and evolution properties of storm cells. We take the snapshots of the simulated storm systems at the interval of 1-hour from different WRF simulations. Moderately moistening the atmosphere (i.e., the RH40 simulation) leads to slightly increased convective intensity (represented by maximum reflectivity and echo top height, Fig. 14c and 14e), while the normalized frequencies of storm size (Fig. 14a) and the total number of convective storm cells (N=4328) do not show notable differences from the CTRL simulation (N=4524). Similar is true for the RH70 simulation, except that the number of storm cells is greatly reduced by 22 % (N=3564). When the atmosphere is saturated (i.e., RH100 simulation), however, we observe more storm cells of smaller volumes (less than 20 km^3) and lower intensities, i.e., maximum reflectivity below 50 dBZ and echo top height less than 4 km. The total number of storm cells is reduced by 60 % for the RH100 simulation (N=1783), the smallest among the three moisture-perturbation scenarios. The increased proportion of storm cells with lower intensities is at the cost of reduced storm cells with moderate intensities. For instance, the proportion of storm cells with echo top between 4-6 km is below 25 % for the RH100 simulation, in contrast to more than 35 % for the CTRL or RH40 simulation (Fig. 14e). This highlight the role of a saturated atmosphere in constraining atmospheric instability and convection. The reduced number of storm cells contribute to the decreased occurrence frequency of convective activities and the spatial coverage of heavy rainfall (Fig. 4d) as well as its magnitudes (Fig. 13) for the RH100 simulation. Despite the contrasts in storm structures, the response of storm evolution (represented by the moving speed of individual storm cells) is consistent under three moisture-perturbation scenarios (Fig. 14g). Moistening the atmosphere leads to increased percentages of fast-moving storm cells (exceeding 30 km h^{-1}). This might be favorable for reducing potentials for severe flash floods over small watersheds (e.g., Doswell et al., 1996; ten Veldhuis et al., 2018), but need to be comprehensively evaluated by considering changes in convective intensity as well.

Increases in temperature do not lead to significant difference in the distributions of storm volume, maximum reflectivity and storm evolution (Fig. 14). However, there are notable shifts in the distribution of the echo top height towards the higher end when the temperature is gradually increased (Fig. 14f). This is consistent with the progressive reduction of ARF at 3-hour and 6-hour and over 100 km^2 (Table 2). These results indicate a stronger potential for deep convection and elevated rain rates at short durations and more severe flash flood hazards.

5.3 Large-scale precipitation efficiency

We examine large-scale precipitation efficiency (PE) over the inner domain for the CTRL simulation and under different moisture and warming scenarios. Large-scale precipitation efficiency is defined as the ratio of the precipitation rate to the sum of all precipitation sources (Braham, 1952). The calculation of PE is as follows (e.g., Sui et al., 2007):

$$\mathrm{PE} = \frac{P_S}{\sum_{i=1}^{4} sgn(Q_i) Q_i} \tag{2}$$

Where $Q_i = (Q_{WVT}, Q_{WVF}, Q_{WVE}, Q_{CM})$; $Q_i > 0$: $sgn\ (Q_i)=1$; $Q_i < 0$: $sgn\ (Q_i)=0$. P_S, Q_{WVT}, Q_{WVF}, Q_{WVE}, Q_{CM} are domain-averaged quantities from model output including precipitation, local vapor change, vapor convergence, evaporation, hydrometeor convergence and local hydrometeor change. Note that the calculation neglects the negative source terms of Q_i.

The 20 July 2021 storm demonstrates extremely high PE, i.e., 0.91 for the CTRL simulation. This is mainly associated with its extreme wet synoptic environment (i.e., with maximum precipitable water exceeding 60 mm) and the low lifting condensation level (around 992 hPa) or the level of free convection (around 988 hPa) (Su et al., 2021). Increases in atmospheric moisture content do not lead to substantial variations in PE. For instance, the PE value for the RH40, RH70, and RH100 simulation is 0.92, 0.92, and 0.90, respectively. By contrast, increases in air temperature lead to gradual increased PE for the particular storm event. The PE value for the AirT1, AirT2, and AirT3 is 0.91, 0.94, and 0.97, respectively. This gives us approximately 3% increase in PE for every 1 °C increase in air temperature. The increased PE under different warming scenarios might be due to the changes in the efficiency of cloud condensation or re-evaporation of falling precipitation (Li et al., 2022; Lutsko & Cronin, 2018). Neither changes in air temperature or atmophseric moisture induce notable changes in the vertical wind shear intensity (i.e., around 4.2 m m s^{-1} between 850 hPa and 500 hPa). This indicates that the meso-scale structure of the storm systems is overall maintained across scenarios. Little variations in PE under different moisture-perturbation scenarios also highlight that it is a reasonable assumption for the conventional approach of PMP estimates to adopt a constant PE during the storm maximization or storm transposition processes. However, it would be necessary to increase PE accordingly when the storm demonstrates a notable signature of anthropogenic climate warming.

6. Summary and Conclusions

In this study, we investigate the 20 July 2021 storm that defines the upper tail of rainfall intensity spectrum over China based on dense, in-situ rainfall observations and high-resolution WRF model simulations. We examine the response of spatial and temporal rainfall variability from this particular storm to atmospheric warming and wetting by modifying the corresponding thermodynamic variables in the model's initial and boundary conditions. The major findings are summarized as follows.

1) The 20 July 2021 storm demonstrates a combination of multi-scale favorable ingredients for extreme rainfall over central and northern China. A prominent synoptic feature of the storm is the remote moisture transport associated with typhoon In-fa (2021). The synoptic-scale feature resembles several historical storms that produced record-breaking rainfall and flood records over China, including the 8 August 1963 storm over the Hai River basin and the 7 August 1975 storm over the upper Huai River basin.

2) The WRF simulation with default initial and boundary conditions (i.e., the CTRL simulation) reasonably captures the spatial and temporal rainfall variability of the 20 July 2021 storm, even though the simulated maximum hourly rain rate shows a moderate underestimation compared to observations. The simulated storm center is about 50 km offset towards west of the observation, but

is still located within the municipal boundary of Zhengzhou. The simulation biases highlight the challenge of existing convection-permitting models in capturing fine-scale extreme rain rates that is responsible for the upper tail of the rainfall intensity spectrum.

3) There are limited variations in the domain-averaged rain rates when the atmospheric moisture content is increased, while the spatial coverage of heavy rainfall (i.e., with hourly rain rate exceeding 20 mm/h) and the peak rain rates show non-monotonic changes to atmospheric moisture content. The most extreme rain rate is produced when there is only moderate moistening to the atmosphere (with relative humidity increased by 20~40 %). The non-monotonic rainfall response to atmospheric moisture content is tied to thermodynamic changes (i.e., CAPE) together with the associated feedbacks from atmospheric dynamics (e.g., moist convergence).

4) The comparable domain-average spatial and temporal rainfall variability under different temperature-perturbation scenarios point to the inertia of large-scale atmospheric dynamics with atmospheric warming, despite the domain-average rain intensity approximately following the Clausius-Clapeyron rate. Rainfall intensity at small spatial scales and short-durations demonstrate non-monotonic response to the increases in temperature, with temperature increment less than 2 °C exhibiting the most notable increased rainfall intensity.

5) Storm tracking analyses reveal contrasting responses of rainfall structures at short durations (less than 6 hours) to the individual changes in atmospheric moisture content and air temperature. The contrasts further explain the non-monotonic rainfall response at the domain scale. Increased atmospheric moisture content leads to reduced storm moving speed, while temperature increases lead to enhanced convection at the storm cell scale. These findings shed light on the potential impact of thermodynamic changes (e.g., moisture and temperature) on extreme rainfall and flash flood hazards under a changing climate.

6) It is reasonable for the conventional PMP estimation approach to adopt a constant precipitation efficiency. This might be due to the extreme high PE of the storm candidate being examined. The assumption would be violated when the signature of anthropogenic climate warming is notable. It is thus necessary to adopt time-variant PMP estimates for the future flood-control infrastructures designs (e.g., Francois et al., 2019).

Our modeling analyses of the 20 July 2021 storm under both the “real-world” condition and different moisture/temperature perturbations scenarios highlight the challenge of reliable extreme rainfall projection under a changing climate. The rainfall response demonstrates strong dependency on thermodynamic changes as well as their associated dynamic processes. These components collectively determine the non-monotonic rainfall changes to atmospheric warming and wetting. The impacts of atmospheric warming and wetting on rainfall structures do not demonstrate in a consistent way, especially for extreme rainfall at small spatial scales and short durations. Previous modeling efforts based on global climate models with coarse resolutions thus offer limited implications for hydrologic designs (e.g., design storms/floods) over cities or small basins that are vulnerable to short-duration rainfall extremes and the resultant flash flood hazards. This is evidenced by the contrasting DAD curves demonstrating rainfall changes at various spatial and temporal scales in this study. While conventional PMP estimation seemingly obtains “maximized” storms, there are possibilities that these estimates cannot represent the “worst-case” scenario. Analyses of synthetic storms based on high-resolution numerical simulations can provide physical constraints for the conventional estimates. A caveat of the present study is that only a single storm event is examined. However, we expect that the non-monotonic behaviors would persist, even though the thresholds of moisture and temperature for the maximum rain rates may vary with different storms. Future studies will investigate other storm candidates that are embedded in diverse synoptic contexts.

Acknowledgements

This study is financially supported by the National Natural Science Foundation of China (52009055). The numerical simulations are implemented on the computing facilities in the High Performance Computing Center (HPCC) of Nanjing University.

Open Research

The rainfall accumulation data used for model validation is available through https://figshare.com/articles/dataset/Rainfall_accumulation_data_for_model_validation/21617790. The JRA5 Reanalysis fields are available through https://rda.ucar.edu/datasets/ds628.0/.

References

Abbs, D. J. (1999). A numerical modeling study to investigate the assumptions used in the calculation of probable maximum precipitation. *Water Resources Research*, *35*(3), 785-796.

Afzali-Gorouh, Z., Faridhosseini, A., Bakhtiari, B., Mosaedi, A., & Salehnia, N. (2022). Monitoring and projection of climate change impact on 24-h probable maximum precipitation in the Southeast of Caspian Sea. *Natural Hazards*, *114*(1), 77-99.

Allan, R. P., & Soden, B. J. (2008). Atmospheric warming and the amplification of precipitation extremes. *Science*, *321*(5895), 1481-1484.

Allen, M. R., & Ingram, W. J. (2002). Constraints on future changes in climate and the hydrologic cycle. *Nature*, *419*(6903), 224-232.

Asadieh, B., & Krakauer, N. Y. (2015). Global trends in extreme precipitation: climate models versus observations. *Hydrology and Earth System Sciences*, *19*(2), 877-891.

Ayat, H., Evans, J. P., Sherwood, S. C., & Soderholm, J. (2022). Intensification of subhourly heavy rainfall. *Science (New York, N.Y.)*, *378*(6620), 655-659.

Ban, N., Schmidli, J., & Schar, C. (2014). Evaluation of the convection-resolving regional climate modeling approach in decade-long simulations. *Journal of Geophysical Research-Atmospheres*, *119*(13), 7889-7907.

Beauchamp, J., Leconte, R., Trudel, M., & Brissette, F. (2013). Estimation of the summer-fall PMP and PMF of a northern watershed under a changed climate. *Water Resources Research*, *49*(6), 3852-3862.

Braham, R. R. (1952). The water and energy budgets of the thunderstorm and their relation to thunderstorm development. *Journal of Meteorology*, *9*(4), 227-242.

Breugem, A. J., Wesseling, J. G., Oostindie, K., & Ritsema, C. J. (2020). Meteorological aspects of heavy precipitation in relation to floods - An overview. *Earth-Science Reviews*, *204*, 103171.

Chawla, I., Osuri, K. K., Mujumdar, P. P., & Niyogi, D. (2018). Assessment of the Weather Research and Forecasting (WRF) model for simulation of extreme rainfall events in the upper Ganga Basin. *Hydrology and Earth System Sciences*, *22*(2), 1095-1117.

Chen, X. D., & Hossain, F. (2019). Understanding future safety of dams in a changing climate. *Bulletin of the American Meteorological Society*, *100*(8), 1395-1404.

Dhar, O. N., & Nandargi, S. (1993). Envelope depth-area-duration rain depths for different homogeneous rainstorm zones of the Indian region. *Theoretical and Applied Climatology*, *47*(2), 117-125.

Dixon, M., & Wiener, G. (1993). TITAN - Thunderstorm Identification, Tracking, Analysis, and

Nowcasting - A radar-based methodology. *Journal of Atmospheric and Oceanic Technology*, *10*(6), 785-797.

Doswell, C. A., Brooks, H. E., & Maddox, R. A. (1996). Flash flood forecasting: an ingredientsbased methodology. *Weather Forecast*, *11*, 560-581.

Dyrrdal, A. V., Stordal, F., & Lussana, C. (2018). Evaluation of summer precipitation from EURO-CORDEX fine-scale RCM simulations over Norway. *International Journal of Climatology*, *38*(4), 1661-1677.

Fowler, H. J., Lenderink, G., Prein, A. F., Westra, S., Allan, R. P., Ban, N., . . . Zhang, X. B. (2021). Anthropogenic intensification of short-duration rainfall extremes. *Nature Reviews Earth & Environment*, *2*(2), 107-122.

Francois, B., Schlef, K. E., Wi, S., & Brown, C. M. (2019). Design considerations for riverine floods in a changing climate - A review. *Journal of Hydrology*, *574*, 557-573.

Fu, S. M., Zhang, Y. C., Wang, H. J., Tang, H., Li, W. L., & Sun, J. H. (2022). On the evolution of a long-lived mesoscale convective vortex that acted as a crucial condition for the extremely strong hourly precipitation in Zhengzhou. *Journal of Geophysical Research-Atmospheres*, *127*(11), e2021JD036233.

Gangrade, S., Kao, S. C., Naz, B. S., Rastogi, D., Ashfaq, M., Singh, N., & Preston, B. L. (2018). Sensitivity of probable maximum flood in a changing environment. *Water Resources Research*, *54*(6), 3913-3936.

Guo, X. J., Huang, J. B., Luo, Y., Zhao, Z. C., & Xu, Y. (2016). Projection of precipitation extremes for eight global warming targets by 17 CMIP5 models. *Natural Hazards*, *84*(3), 2299-2319.

Haerter, J. O., & Berg, P. (2009). Unexpected rise in extreme precipitation caused by a shift in rain type? *Nature Geoscience*, *2*(6), 372-373.

Held, I. M., & Soden, B. J. (2006). Robust responses of the hydrological cycle to global warming. *Journal of Climate*, *19*(21), 5686-5699.

Hiraga, Y., Iseri, Y., Warner, M. D., Frans, C. D., Duren, A. M., England, J. F., & Kavvas, M. L. (2021). Estimation of long-duration maximum precipitation during a winter season for large basins dominated by atmospheric rivers using a numerical weather model. *Journal of Hydrology*, *598*, 126224.

Huang, X., Swain, D. L., & Hall, A. D. (2020). Future precipitation increase from very high resolution ensemble downscaling of extreme atmospheric river storms in California. *Science Advances*, *6*(29), eaba1323.

IPCC. (2021). Climate Change 2021: The physical science basis. Contribution of Working Group I to the Sixth Assessment Report of the Intergovernmental Panel on climate change (Vol. In Press). *Cambridge University Press*.

Ishida, K., Kavvas, M. L., Jang, S., Chen, Z. Q., Ohara, N., & Anderson, M. L. (2015a). Physically based estimation of maximum precipitation over three watersheds in Northern California: Relative humidity maximization method. *Journal of Hydrologic Engineering*, *20*(10), 04015014.

Ishida, K., Kavvas, M. L., Jang, S., Chen, Z. Q., Ohara, N., & Anderson, M. L. (2015b). Physically based estimation of maximum precipitation over three watersheds in Northern California: Atmospheric boundary condition shifting. *Journal of Hydrologic Engineering*, *20*(4), 04014052.

Ishida, K., Ohara, N., Kavvas, M. L., Chen, Z. Q., & Anderson, M. L. (2018). Impact of air temperature on physically-based maximum precipitation estimation through change in moisture holding capacity of air. *Journal of Hydrology*, *556*, 1050-1063.

Kendon, E. J., Roberts, N. M., Fowler, H. J., Roberts, M. J., Chan, S. C., & Senior, C. A. (2014). Heavier summer downpours with climate change revealed by weather forecast resolution model. *Nature Climate Change*, *4*(7), 570-576.

Kim, S., Sharma, A., Wasko, C., & Nathan, R. (2022). Linking total precipitable water to precipitation extremes globally. *Earths Future*, *10*(2), e2021EF002473.

Kreibich, H., Van Loon, A. F., Schroeter, K., Ward, P. J., Mazzoleni, M., Sairam, N., . . . Di Baldassarre, G. (2022). The challenge of unprecedented floods and droughts in risk management. *Nature*, *608*(7921), 80-86.

Kreienkamp, F., Philip, S. Y., Tradowsky, J. S., Kew, S. F., Lorenz, P., Arrighi, J., & Wanders, N. (2021). Rapid attribution of heavy rainfall events leading to the severe flooding in Western Europe during July 2021. *World Weather Attribution*.

Kunkel, K. E., Karl, T. R., Easterling, D. R., Redmond, K., Young, J., Yin, X. G., & Hennon, P. (2013). Probable maximum precipitation and climate change. *Geophysical Research Letters*, *40*(7), 1402-1408.

Kunkel, K. E., Stevens, S. E., Stevens, L. E., & Karl, T. R. (2020). Observed climatological relationships of extreme daily precipitation events with precipitable water and vertical velocity in the contiguous United States. *Geophysical Research Letters*, *47*(12), e2019GL086721.

Li, R. L., Studholme, J. H. P., Fedorov, A. V., & Storelvmo, T. (2022). Precipitation efficiency constraint on climate change. *Nature Climate Change*, *12*(7), 642-648.

Li, S. S., Li, G. P., Wang, X. F., Li, C., Liu, H. Z., & Li, G. (2020). Precipitation characteristics of an abrupt heavy rainfall event over the complex terrain of southwest China observed by the FY-4A Satellite and Doppler weather radar. *Water*, *12*(9), 2502.

Liang, X. D., Xia, R. D., Bao, X. H., Zhang, X., Wang, X. M., Su, A. F., . . . Chen, L. J. (2022). Preliminary investigation on the extreme rainfall event during July 2021 in Henan Province and its multi-scale processes. *Chinese Science Bulletin-Chinese*, *67*(10), 997-1011.

Lochbihler, K., Lenderink, G., & Siebesma, A. P. (2017). The spatial extent of rainfall events and its relation to precipitation scaling. *Geophysical Research Letters*, *44*(16), 8629-8636.

Lucas-Picher, P., Argueso, D., Brisson, E., Tramblay, Y., Berg, P., Lemonsu, A., . . . Caillaud, C. (2021). Convection-permitting modeling with regional climate models: Latest developments and next steps. *Wiley Interdisciplinary Reviews-Climate Change*, *12*(6), e731.

Luo, Y. L., Gong, Y., & Zhang, D. L. (2014). Initiation and organizational modes of an extreme-rain-producing mesoscale convective system along a Mei-Yu Front in East China. *Monthly Weather Review*, *142*(1), 203-221.

Luo, Y. L., Zhang, J. H., Yu, M., Liang, X. D., Xia, R. D., Gao, Y. Y., . . . Yin, J. F. (2022). On the influences of urbanization on the extreme rainfall over Zhengzhou on 20 July 2021: A convection-permitting ensemble modeling study. *Advances in Atmospheric Sciences*. https://doi.org/10.1007/s00376-022-2048-8

Lutsko, N. J., & Cronin, T. W. (2018). Increase in precipitation efficiency with surface warming in radiative-convective equilibrium. *Journal of Advances in Modeling Earth Systems*, *10*(11), 2992-3010.

Mohan, P. R., Srinivas, C. V., Yesubabu, V., Baskaran, R., & Venkatraman, B. (2018). Simulation of a heavy rainfall event over Chennai in Southeast India using WRF: Sensitivity to microphysics parameterization. *Atmospheric Research*, *210*, 83-99.

Molnar, P., Fatichi, S., Gaal, L., Szolgay, J., & Burlando, P. (2015). Storm type effects on super

Clausius-Clapeyron scaling of intense rainstorm properties with air temperature. *Hydrology and Earth System Sciences*, *19*(4), 1753-1766.

Nie, J., Dai, P. X., & Sobel, A. H. (2020). Dry and moist dynamics shape regional patterns of extreme precipitation sensitivity. *Proceedings of the National Academy of Sciences of the United States of America*, *117*(16), 8757-8763.

O'Gorman, P. A., & Schneider, T. (2009). The physical basis for increases in precipitation extremes in simulations of 21st-century climate change. *Proceedings of the National Academy of Sciences of the United States of America*, *106*(35), 14773-14777.

Odemark, K., Muller, M., & Tveito, O. E. (2021). Changing lateral boundary conditions for probable maximum precipitation studies: A physically consistent approach. *Journal of Hydrometeorology*, *22*(1), 113-123.

Ohara, N., Kavvas, M. L., Anderson, M. L., Chen, Z. Q., & Ishida, K. (2017). Characterization of extreme storm events using a numerical model-based precipitation maximization procedure in the Feather, Yuba, and American River Watersheds in california. *Journal of Hydrometeorology*, *18*(5), 1413-1423.

Ohara, N., Kavvas, M. L., Kure, S., Chen, Z. Q., Jang, S., & Tan, E. (2011). Physically based estimation of maximum precipitation over American River Watershed, California. *Journal of Hydrologic Engineering*, *16*(4), 351-361.

Pall, P., Allen, M. R., & Stone, D. A. (2007). Testing the Clausius-Clapeyron constraint on changes in extreme precipitation under CO2 warming. *Climate Dynamics*, *28*(4), 351-363.

Panthou, G., Mailhot, A., Laurence, E., & Talbot, G. (2014). Relationship between surface temperature and extreme rainfalls: a multi-time-scale and event-based analysis. *Journal of Hydrometeorology*, *15*(5), 1999-2011.

Papalexiou, S. M., & Montanari, A. (2019). Global and regional increase of precipitation extremes under global warming. *Water Resources Research*, *55*(6), 4901-4914.

Patel, P., Ghosh, S., Kaginalkar, A., Islam, S., & Karmakar, S. (2019). Performance evaluation of WRF for extreme flood forecasts in a coastal urban environment. *Atmospheric Research*, *223*, 39-48.

Pendergrass, A. G. (2018). What precipitation is extreme? *Science*, *360*(6393), 1072-1073.

Pendergrass, A. G., Coleman, D. B., Deser, C., Lehner, F., Rosenbloom, N., & Simpson, I. R. (2019). Nonlinear response of extreme precipitation to warming in CESM1. *Geophysical Research*

Letters, *46*(17-18), 10551-10560.

Pennelly, C., Reuter, G., & Flesch, T. (2014). Verification of the WRF model for simulating heavy precipitation in Alberta. *Atmospheric Research*, *135*, 172-192.

Pfahl, S., O'Gorman, P. A., & Fischer, E. M. (2017). Understanding the regional pattern of projected future changes in extreme precipitation. *Nature Climate Change*, *7*(6), 423-427.

Prein, A. F., Holland, G. J., Rasmussen, R. M., Done, J., Ikeda, K., Clark, M. P., & Liu, C. H. H. (2013). Importance of regional climate model grid spacing for the simulation of heavy precipitation in the Colorado Headwaters. *Journal of Climate*, *26*(13), 4848-4857.

Prein, A. F., Langhans, W., Fosser, G., Ferrone, A., Ban, N., Goergen, K., . . . Leung, R. (2015). A review on regional convection-permitting climate modeling: Demonstrations, prospects, and challenges. *Reviews of Geophysics*, *53*(2), 323-361.

Prein, A. F., Rasmussen, R. M., Ikeda, K., Liu, C. H., Clark, M. P., & Holland, G. J. (2017). The future intensification of hourly precipitation extremes. *Nature Climate Change*, *7*(1), 48-52.

Rajeevan, M., Kesarkar, A., Thampi, S. B., Rao, T. N., Radhakrishna, B., & Rajasekhar, M. (2010). Sensitivity of WRF cloud microphysics to simulations of a severe thunderstorm event over Southeast India. *Annales Geophysicae*, *28*(2), 603-619.

Rastogi, D., Kao, S. C., Ashfaq, M., Mei, R., Kabela, E. D., Gangrade, S., . . . Anantharaj, V. G. (2017). Effects of climate change on probable maximum precipitation: A sensitivity study over the Alabama-Coosa-Tallapoosa River Basin. *Journal of Geophysical Research-Atmospheres*, *122*(9), 4808-4828.

Salas, J. D., Anderson, M. L., Papalexiou, S. M., & Frances, F. (2020). PMP and climate variability and change: A review. *Journal of Hydrologic Engineering*, *25*(12), 03120002.

Schar, C., Frei, C., Luthi, D., & Davies, H. C. (1996). Surrogate climate-change scenarios for regional climate models. *Geophysical Research Letters*, *23*(6), 669-672.

Skamarock, W. C., Klemp, J. B., Dudhia, J., Gill, D. O., Liu, Z., Berner, J., . . . Huang, X.-Y. (2021). A Description of the Advanced Research WRF Model Version 4.3. *NCAR Technical Note NCAR/TN-556+STR*.

Stanski, H. R., Wilson, L. J., & Burrows, W. R. (1989). Survey of common verification methods in meteorology (Vol. TD No. 358). *World Meteorological Organization*.

Su, A. F., Lyu, X. N., Cui, L. M., Li, Z., Xi, L., & Li, H. (2021). The Basic Observational Analysis of

"7.20" Extreme Rainstorm in Zhengzhou. *Torrential Rain and Disasters*, *40*(5), 445-454.

Sui, C. H., Li, X. F., & Yang, M. J. (2007). On the definition of precipitation efficiency. *Journal of the Atmospheric Sciences*, *64*(12), 4506-4513.

Svensson, C., & Rakhecha, P. R. (1998). Estimation of probable maximum precipitation for dams in the Hongru river catchment, China. *Theoretical and Applied Climatology*, *59*(1-2), 79-91.

ten Veldhuis, M.-c., Zhou, Z., Yang, L., Liu, S., & Smith, J. (2018). The role of storm scale, position and movement in controlling urban flood response. *Hydrology and Earth System Sciences*, *22*(1), 417-436.

Terzago, S., Palazzi, E., & von Hardenberg, J. (2018). Stochastic downscaling of precipitation in complex orography: a simple method to reproduce a realistic fine-scale climatology. *Natural Hazards and Earth System Sciences*, *18*(11), 2825-2840.

Tewari, M., Chen, F., Dudhia, J., Ray, P., Miao, S. G., Nikolopoulos, E., & Treinish, L. (2022). Understanding the sensitivity of WRF hindcast of Beijing extreme rainfall of 21 July 2012 to microphysics and model initial time. *Atmospheric Research*, *271*, 106085.

Toride, K., Iseri, Y., Warner, M. D., Frans, C. D., Duren, A. M., England, J. F., & Kavvas, M. L. (2019). Model-based probable maximum precipitation estimation: How to estimate the worst-case scenario induced by atmospheric rivers? *Journal of Hydrometeorology*, *20*(12), 2383-2400.

Trenberth, K. E., Dai, A., Rasmussen, R. M., & Parsons, D. B. (2003). The changing character of precipitation. *Bulletin of the American Meteorological Society*, *84*(9), 1205-1217.

Utsumi, N., Seto, S., Kanae, S., Maeda, E. E., & Oki, T. (2011). Does higher surface temperature intensify extreme precipitation? *Geophysical Research Letters*, *38*, L16708.

Wang, C. C. (2014). On the calculation and correction of equitable threat score for model quantitative precipitation forecasts for small verification areas: The example of Taiwan. *Weather and Forecasting*, *29*(4), 788-798.

Wang, J., Chen, Y., Nie, J., Yan, Z., Zhai, P., & Feng, J. (2022). On the role of anthropogenic warming and wetting in the July 2021 Henan record-shattering rainfall. *Science Bulletin*, *67*(20), 2055-2059.

Wasko, C., & Sharma, A. (2015). Steeper temporal distribution of rain intensity at higher temperatures within Australian storms. *Nature Geoscience*, *8*(7), 527-529.

Wasko, C., Sharma, A., & Johnson, F. (2015). Does storm duration modulate the extreme precipitation-temperature scaling relationship? *Geophysical Research Letters*, *42*(20), 8783-8790.

Wasko, C., Sharma, A., & Westra, S. (2016). Reduced spatial extent of extreme storms at higher temperatures. *Geophysical Research Letters*, *43*(8), 4026-4032.

Weisman, M. L., Skamarock, W. C., & Klemp, J. B. (1997). The resolution dependence of explicitly modeled convective systems. *Monthly Weather Review*, *125*(4), 527-548.

Westra, S., Fowler, H. J., Evans, J. P., Alexander, L. V., Berg, P., Johnson, F., . . . Roberts, N. M. (2014). Future changes to the intensity and frequency of short-duration extreme rainfall. *Reviews of Geophysics*, *52*(3), 522-555.

Wilks, D. S. (1995). Statistical Methods in the Atmospheric Sciences. An Introduction. *Academic Press*.

World Meteorological Organization. (2009). Manual on estimation of probable maximum precipitation (PMP) (Vol. WMO-no. 1045). *World Meteorological Organization*.

Xu, H. X., Duan, Y. H., Li, Y., & Wang, H. (2022). Indirect effects of binary typhoons on an extreme rainfall event in Henan Province, China from 19 to 21 July 2021: 2. Numerical study. *Journal of Geophysical Research-Atmospheres*, *127*(15), e2021JD036083.

Xu, H. X., Duan, Y. H., & Xu, X. D. (2022). Indirect effects of binary typhoons on an extreme rainfall event in Henan Province, China from 19 to 21 July 2021: 1. Ensemble-based analysis. *Journal of Geophysical Research-Atmospheres*, *127*(10), e2021JD036265.

Yang, L., Liu, M. F., Smith, J. A., & Tian, F. Q. (2017). Typhoon Nina and the August 1975 Flood over Central China. *Journal of Hydrometeorology*, *18*(2), 451-472.

Yang, L., Ni, G. H., Tian, F. Q., & Niyogi, D. (2021). Urbanization exacerbated rainfall over European suburbs under a warming climate. *Geophysical Research Letters*, *48*(21), e2021GL095987.

Yang, L., & Smith, J. (2018). Sensitivity of extreme rainfall to atmospheric moisture content in the arid/semiarid southwestern United States: Implications for probable maximum precipitation estimates. *Journal of Geophysical Research-Atmospheres*, *123*(3), 1638-1656.

Yang, L., Yang, Y. X., & Smith, J. (2021). The upper tail of flood peaks over China: Hydrology, hydrometeorology, and hydroclimatology. *Water Resources Research*, *57*(11), e2021WR030883.

Yin, J. F., Gu, H. D., Liang, X. D., Yu, M., Sun, J. S., Xie, Y. X., . . . Wu, C. (2022). A possible dynamic mechanism for rapid production of the extreme hourly rainfall in Zhengzhou City on 20 July 2021. *Journal of Meteorological Research*, *36*(1), 6-25.

Yu, R. C., Zhou, T. J., Xiong, A. Y., Zhu, Y. J., & Li, J. M. (2007). Diurnal variations of summer precipitation over contiguous China. *Geophysical Research Letters*, *34*(1), L01704.

Yu, Y., Gao, T., Xie, L., Zhang, R.-H., Zhang, W., Xu, H., . . . Chen, B. (2022). Tropical cyclone over the western Pacific triggers the record-breaking '21/7' extreme rainfall in Henan, central-eastern China. *Environmental Research Letters*, *17*(12), 124003.

Zhang, S. H., Chen, Y. R. X., Luo, Y. L., Liu, B., Ren, G. Y., Zhou, T. J., . . . Chang, M. Y. (2022). Revealing the circulation pattern most conducive to precipitation extremes in Henan Province of North China. *Geophysical Research Letters*, *49*(7), e2022GL098034.

Zhang, T. J., Li, Y. H., Duan, H. X., Liu, Y. P., Zeng, D. W., Zhao, C. L., . . . Yan, P. C. (2019). Development and evaluation of a WRF-based mesoscale numerical weather prediction system in Northwestern China. *Atmosphere*, *10*(6), 344.

Zhao, W. J., Smith, J. A., & Bradley, A. A. (1997). Numerical simulation of a heavy rainfall event during the PRE-STORM experiment. *Water Resources Research*, *33*(4), 783-799.

Zhu, K., Zhang, C., Xue, M., & Yang, N. (2022). Predictability and skill of convection-permitting ensemble forecast systems in predicting the record-breaking "21·7" extreme rainfall event in Henan Province, China. *Science China Earth Sciences*, *65*(10), 1879-1902.

List of tables

Table 1. Details of all simulations implemented in this study.

Scenarios	Short name	Adjustment	Objectives
Control simulation	CTRL	/	To evaluate the model's performance
Moisture-perturbation simulations	RH10	α=0.1	To examine the rainfall response to the changes in atmospheric moisture content
	RH20	α=0.2	
	……	……	
	RH100	α=1.0	
Temperature-perturbation simulations	AirT1	ΔT=1	To examine the rainfall response to the changes in air temperature
	AirT2	ΔT=2	
	AirT1	ΔT=3	

Table 2. Areal reduction factors (ARF) of different durations under different WRF scenarios.

	100 km^2			1000 km^2			10000 km^2		
	3 hrs	6 hrs	12 hrs	3 hrs	6 hrs	12 hrs	3 hrs	6 hrs	12 hrs
CTRL	0.8	0.86	0.9	0.42	0.49	0.58	0.19	0.23	0.33
RH40	0.89	0.9	0.9	0.5	0.59	0.65	0.24	0.35	0.41
RH70	0.82	0.74	0.84	0.56	0.48	0.64	0.27	0.24	0.37
RH100	0.8	0.82	0.84	0.44	0.54	0.59	0.13	0.2	0.24
AirT1	0.79	0.77	0.76	0.3	0.33	0.42	0.11	0.14	0.24
AirT2	0.74	0.75	0.83	0.46	0.47	0.63	0.23	0.26	0.37
AirT3	0.64	0.68	0.74	0.26	0.37	0.43	0.11	0.17	0.23

List of Figures

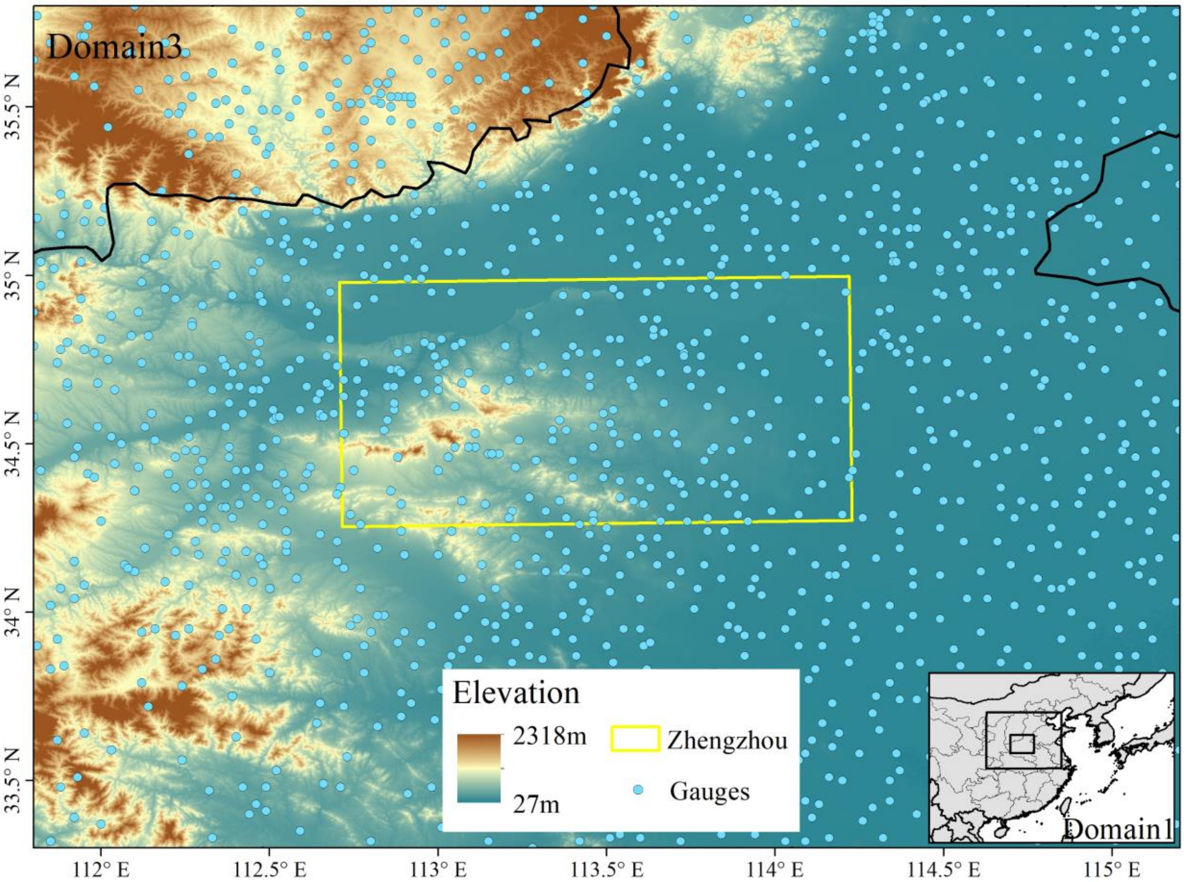

Figure 1. Map of the study region. The black line shows the boundary of Henan province. The yellow line represents the spatial extent of the Zhengzhou city. Blue dots represent the rain gauges, with shade represent topography. The insert map shows the three nested domains of the WRF simulations.

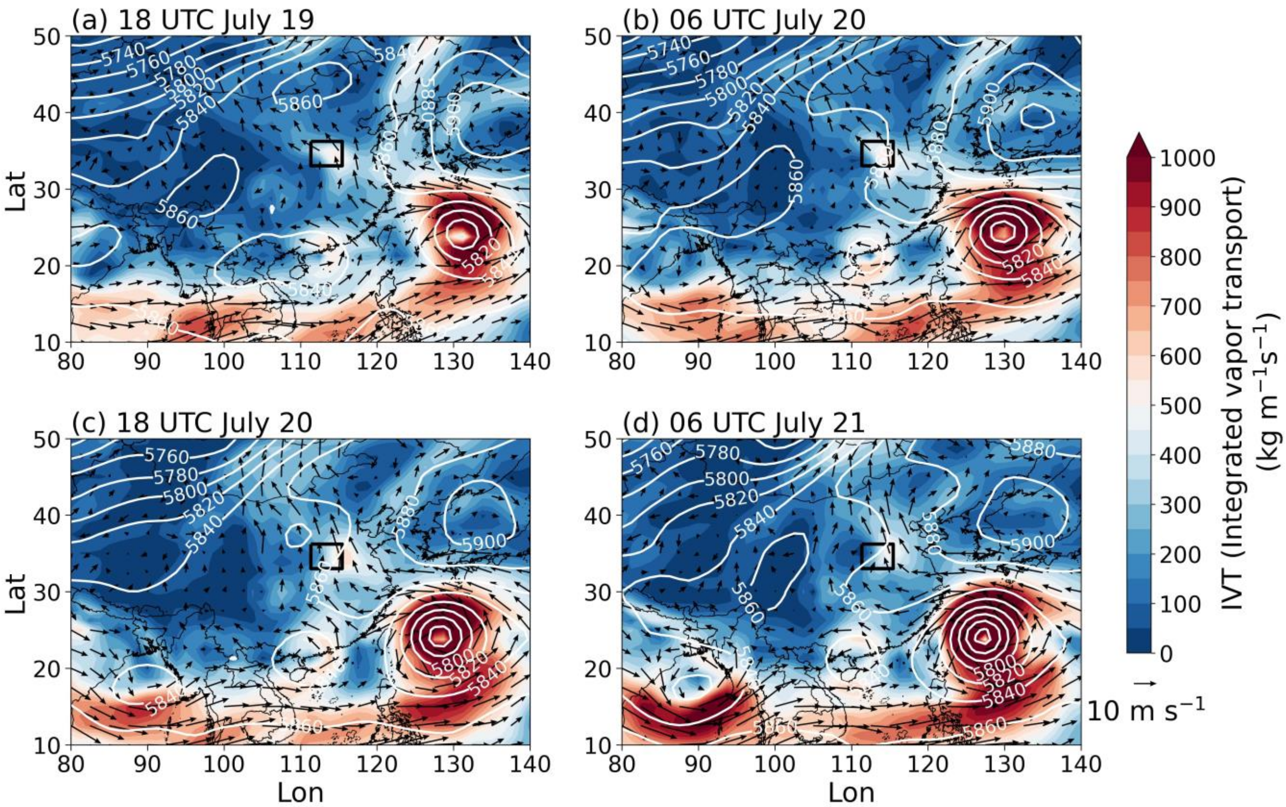

Figure 2. Synoptic conditions at (a) 18 UTC 19 July, (b) 06 UTC 19 July and (c) 18 UTC 20 July, and (d) 06 UTC 21 July. Geopotential height at 500 hPa (contours, in geopotential meters), wind fields at 700 hPa (vectors, in m s^{-1}), and IVT (shaded, in kg m^{-1} s^{-1}). The black box show domain 3. Black lines show the national boarder. These synoptic fields are extracted from the JRA 55 reanalysis fields.

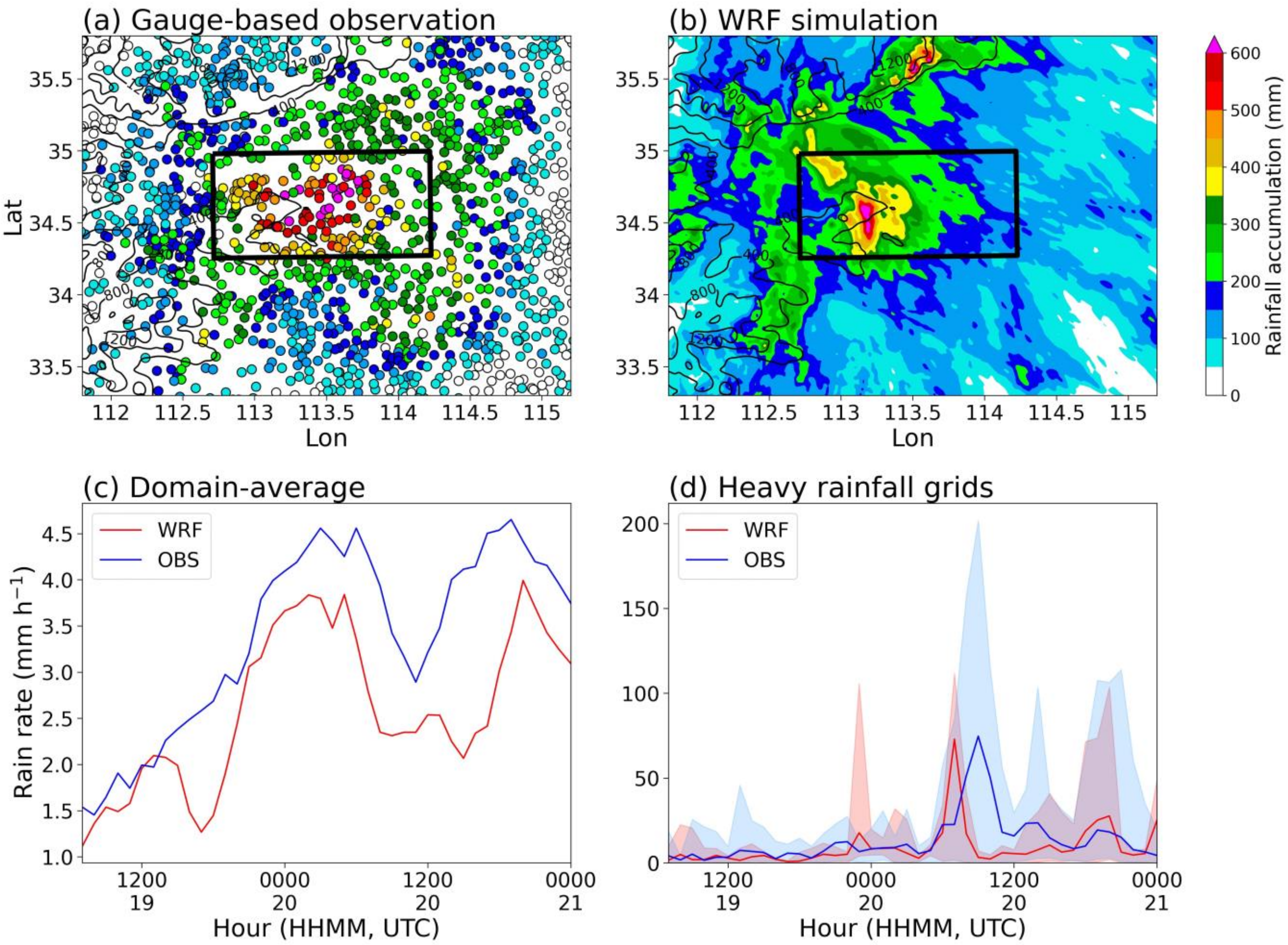

Figure 3. Comparisons of rainfall accumulation between the CTRL simulation and rain gauge observations during the period 06 UTC 19 July - 00 UTC 21 July 2021. (a) Gauge-based and (b) simulated rainfall accumulation (in mm). The black box represents the Zhengzhou city. The contours represent the topography with an interval of 200 meters. (c) Time series of domain-average rain rate. (d) Time series of rain rate for the rain gauge and model grids with the maximum hourly fall exceeding 100 mm h^{-1}. The solid lines represent the ensemble mean rain rate, with the shading representing the range.

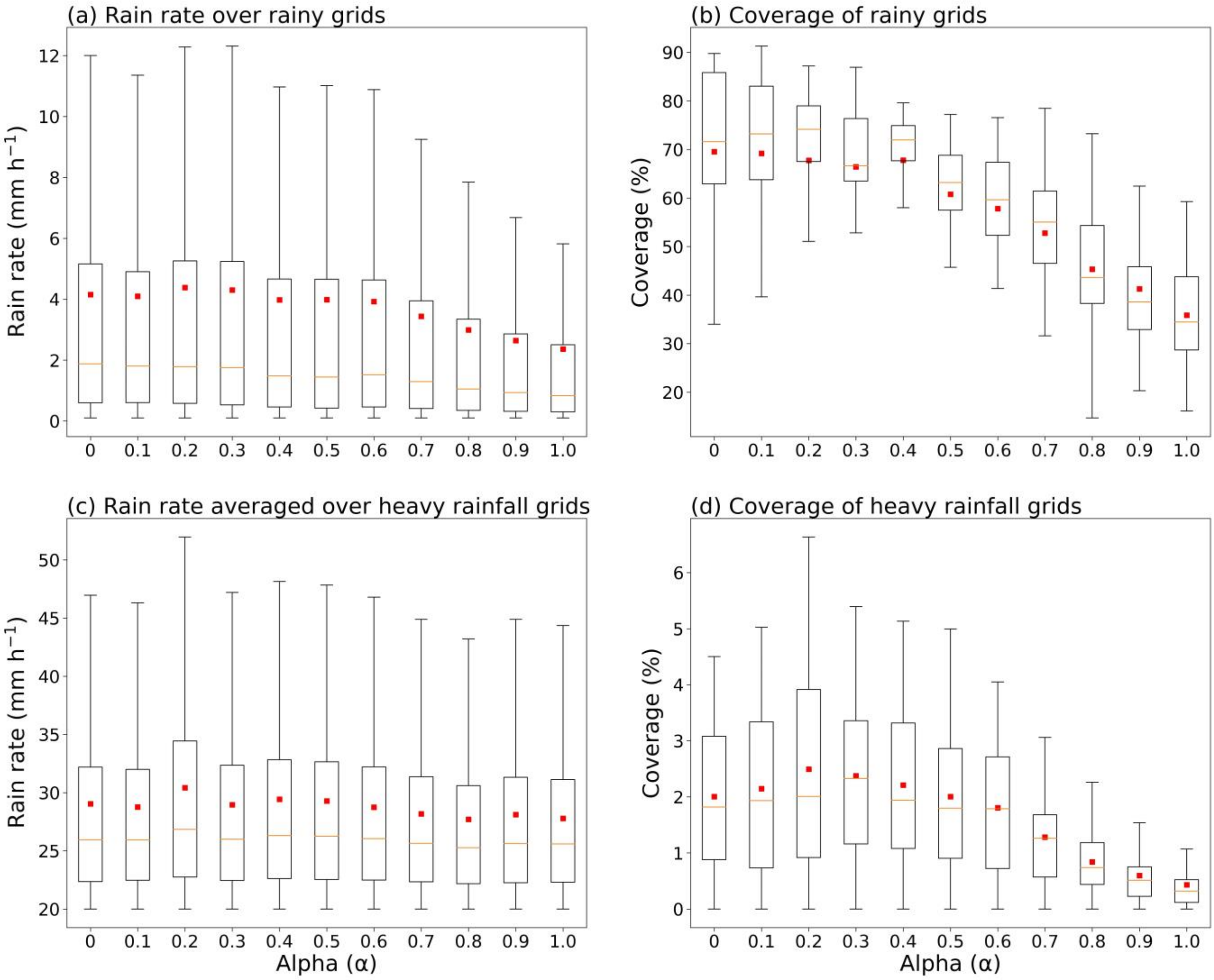

Figure 4. Boxplots of rain rate averaged (a) over all rainy grids (exceeding 0.1 mm h^{-1}) and (c) over the grids with rain rate exceeding 20 mm h^{-1} under different moisture conditions (represented by different amplification factors). Boxplots of the spatial coverage of (b) rainy grids and (d) the grids with rain rate exceeding 20 mm h^{-1}. The spatial coverage is represented by the number of qualified grids divided by the total number of grids within domain 3. The box spans the 25th and 75th percentiles, and the whiskers represent 5th and 95th percentiles. The yellow lines and red squares in the box represent the median and mean values, respectively.

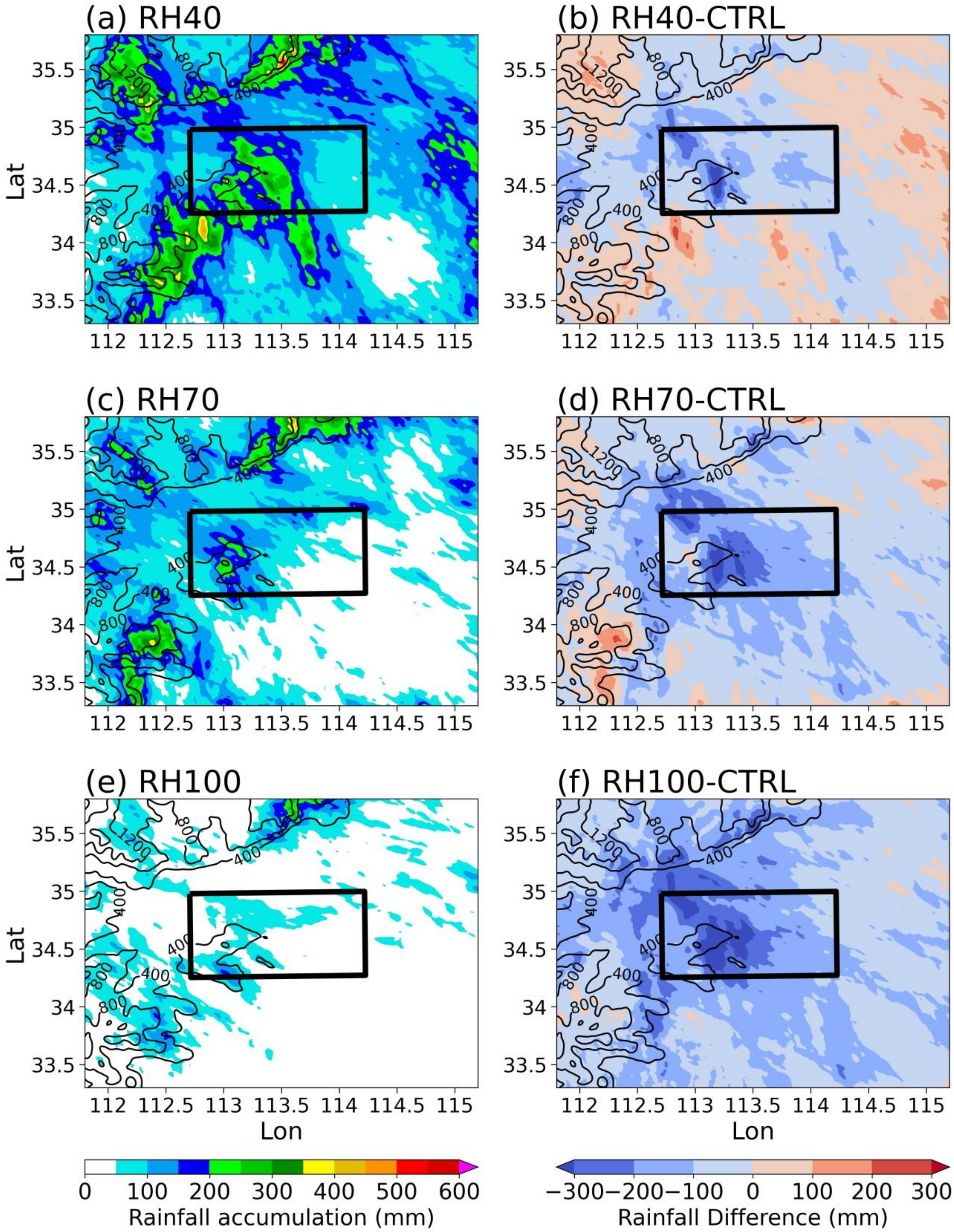

Figure 5. Spatial patterns of rainfall accumulation for three moisture-perturbation scenarios (a, c, e) and their difference from the CTRL simulation (b, d, f) during the period 06 UTC 19 July - 00 UTC 21 July 2021. The black box represents the Zhengzhou city. The contours represent the topography with an interval of 400 meters.

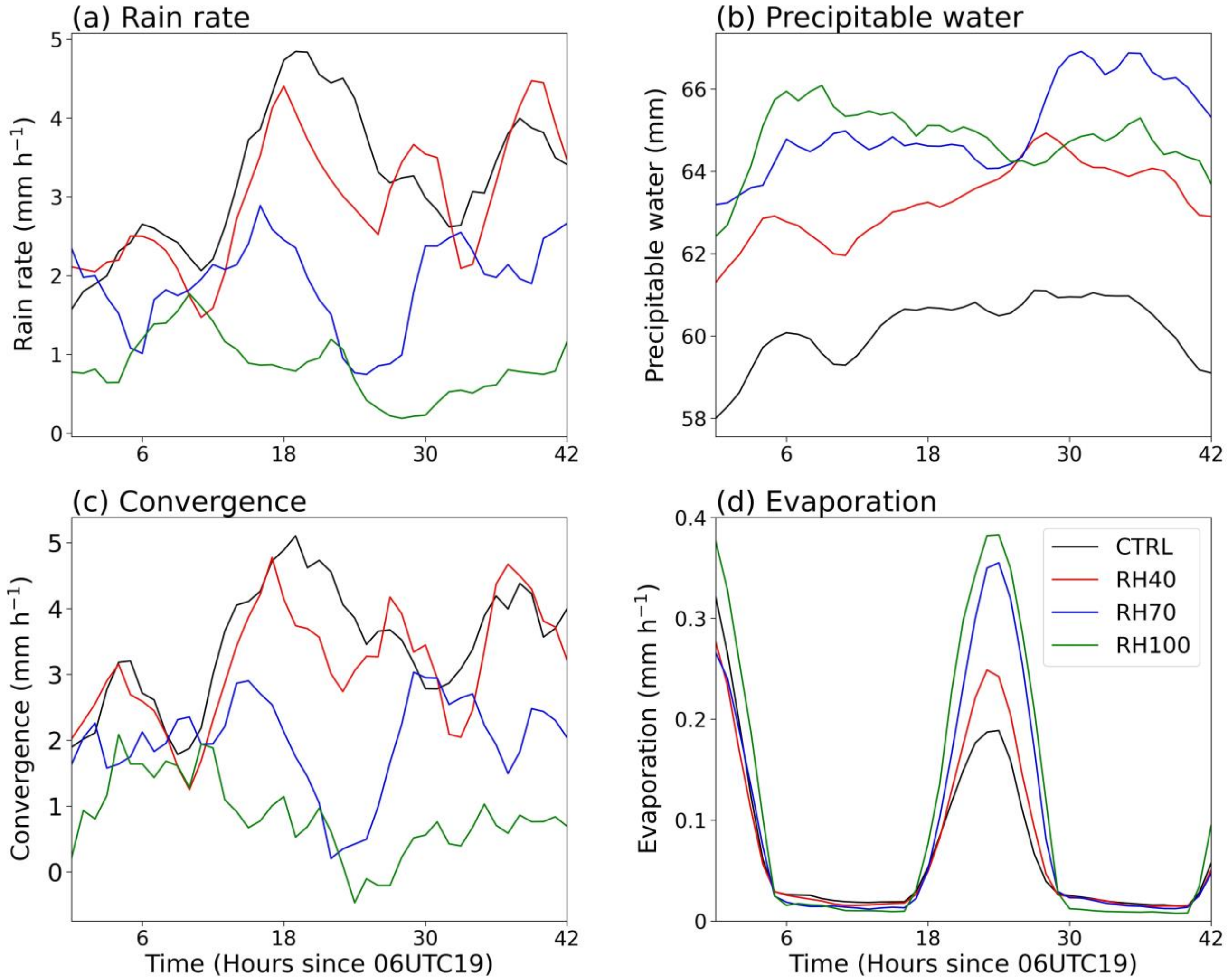

Figure 6. Time series of domain-average (a) rain rate (in mm h^{-1}), (b) precipitable water (in mm), (c) convergence of water vapor (in mm h^{-1}), and (d) evaporation rate (in mm h^{-1}) for the CTRL simulation and three moisture-perturbation scenarios.

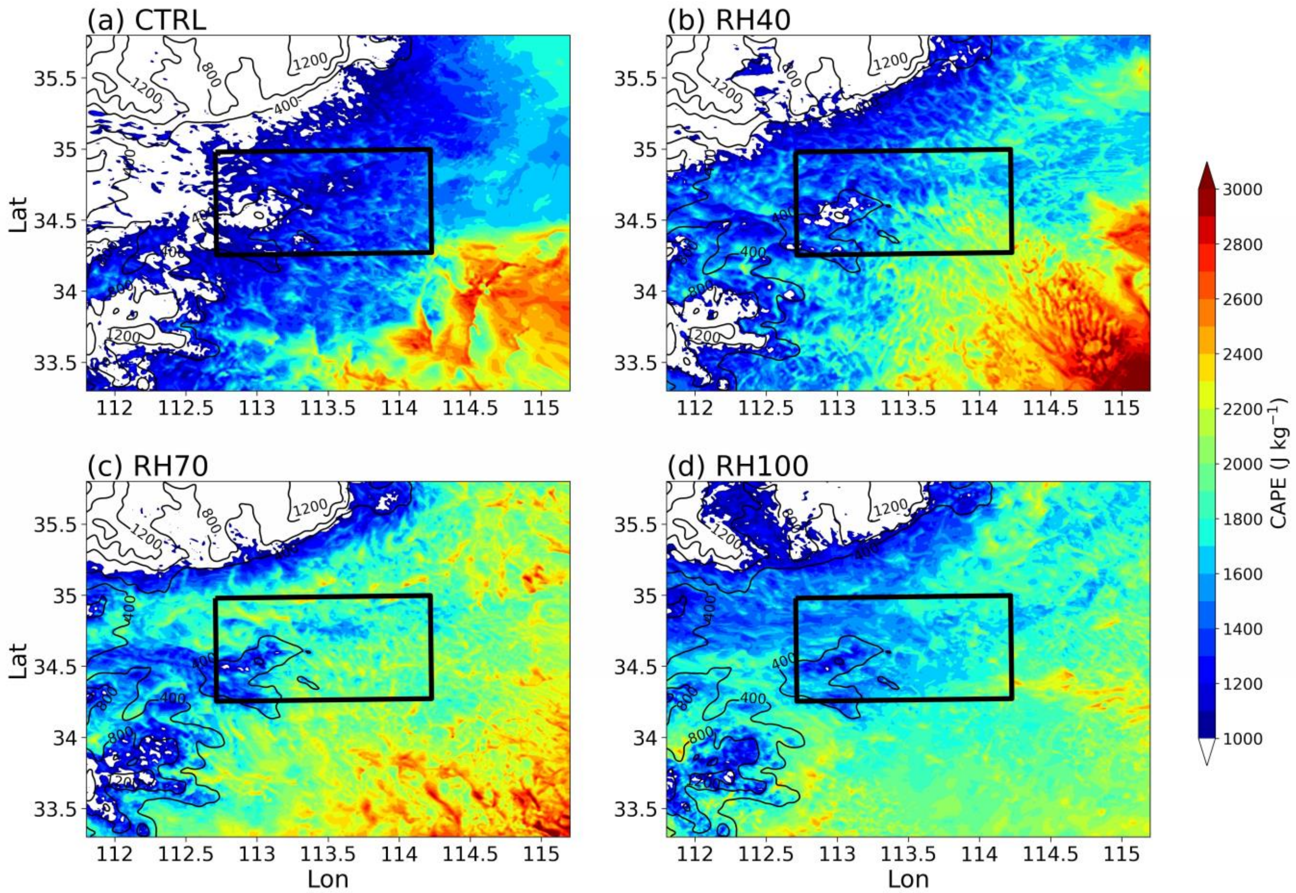

Figure 7. Spatial distribution of the maximum CAPE during the entire storm period for (a) CTRL, (b) RH40, (c) RH70, and (d) RH100 simulation. The black box represents the Zhengzhou city. The contours represent the topography with an interval of 200 meters.

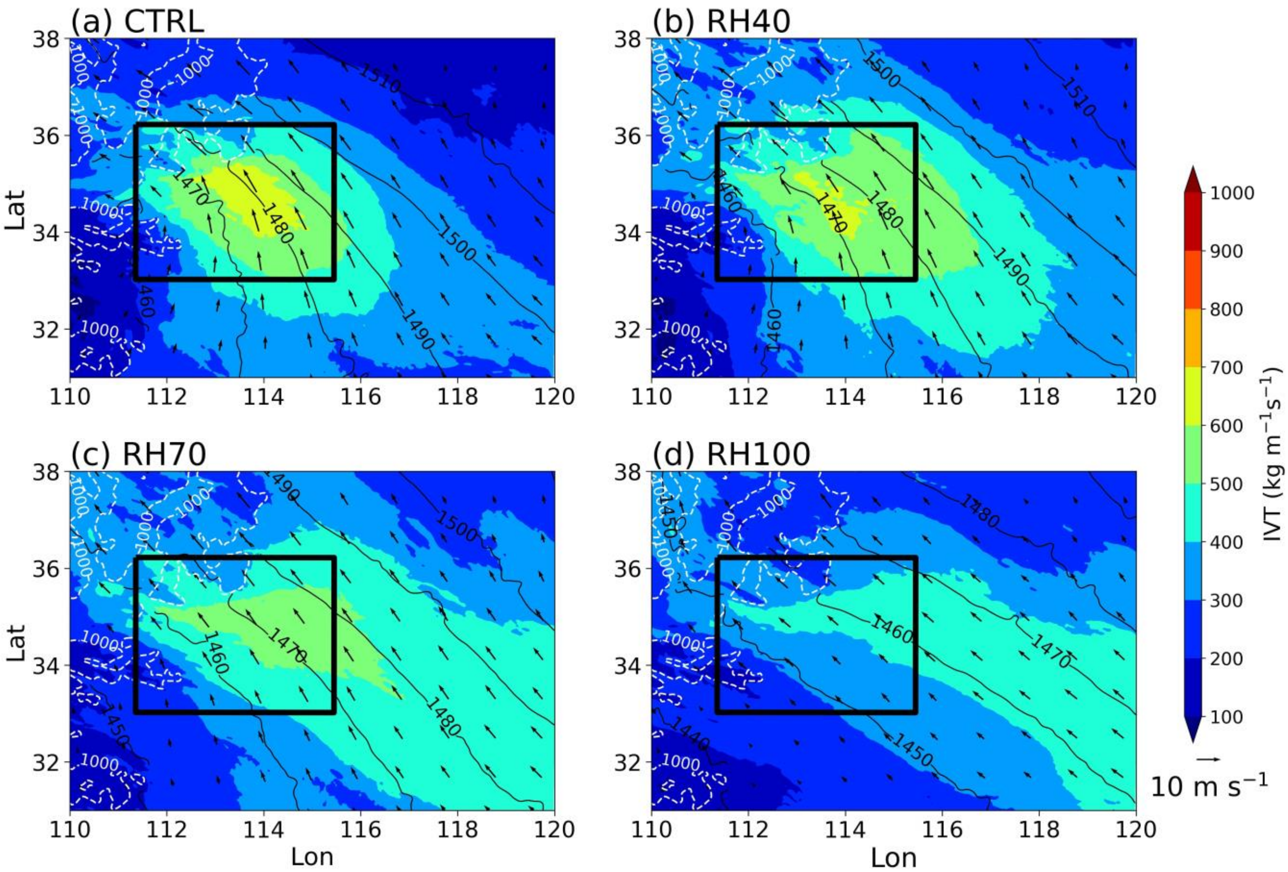

Figure 8. The spatial pattern of time-average integrated water vapor transport (shaded, in kg m^{-1} s^{-1}) during the study period for the (a) CTRL, (b) RH40, (c) RH70, and (d) RH100 simulation. The contours show the time-average geopotential height at 850 hPa (in geopotential meters), while the vectors represent mean steering-level wind at 700 hPa (in m s^{-1}). The black box shows the boundary of domain 3. The white dashed contours show the topography with an interval of 1000 meters.

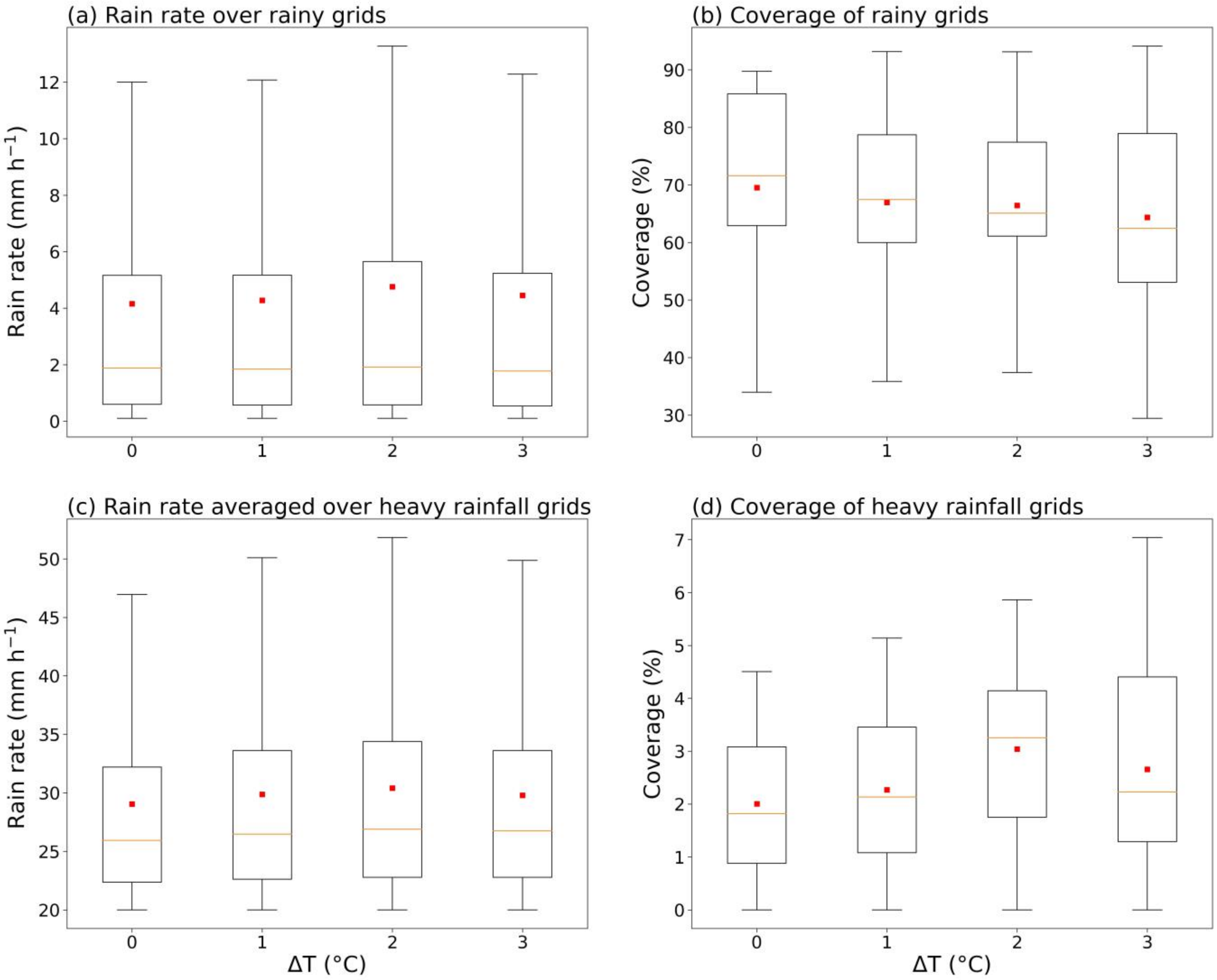

Figure 9. Boxplots of rain rate averaged (a) over all rainy grids (exceeding 0.1 mm h^{-1}) and (c) over the grids with rain rate exceeding 20 mm h^{-1} under different temperature conditions (represented by different values of the temperature increment). Boxplots of the spatial coverage of (b) rainy grids and (d) the grids with rain rate exceeding 20 mm h^{-1}. The spatial coverage is represented by the number of qualified grids divided by the total number of grids within domain 3. The box spans the 25th and 75th percentiles, and the whiskers represent 5th and 95th percentiles. The yellow lines and red squares in the box represent the median and mean values, respectively.

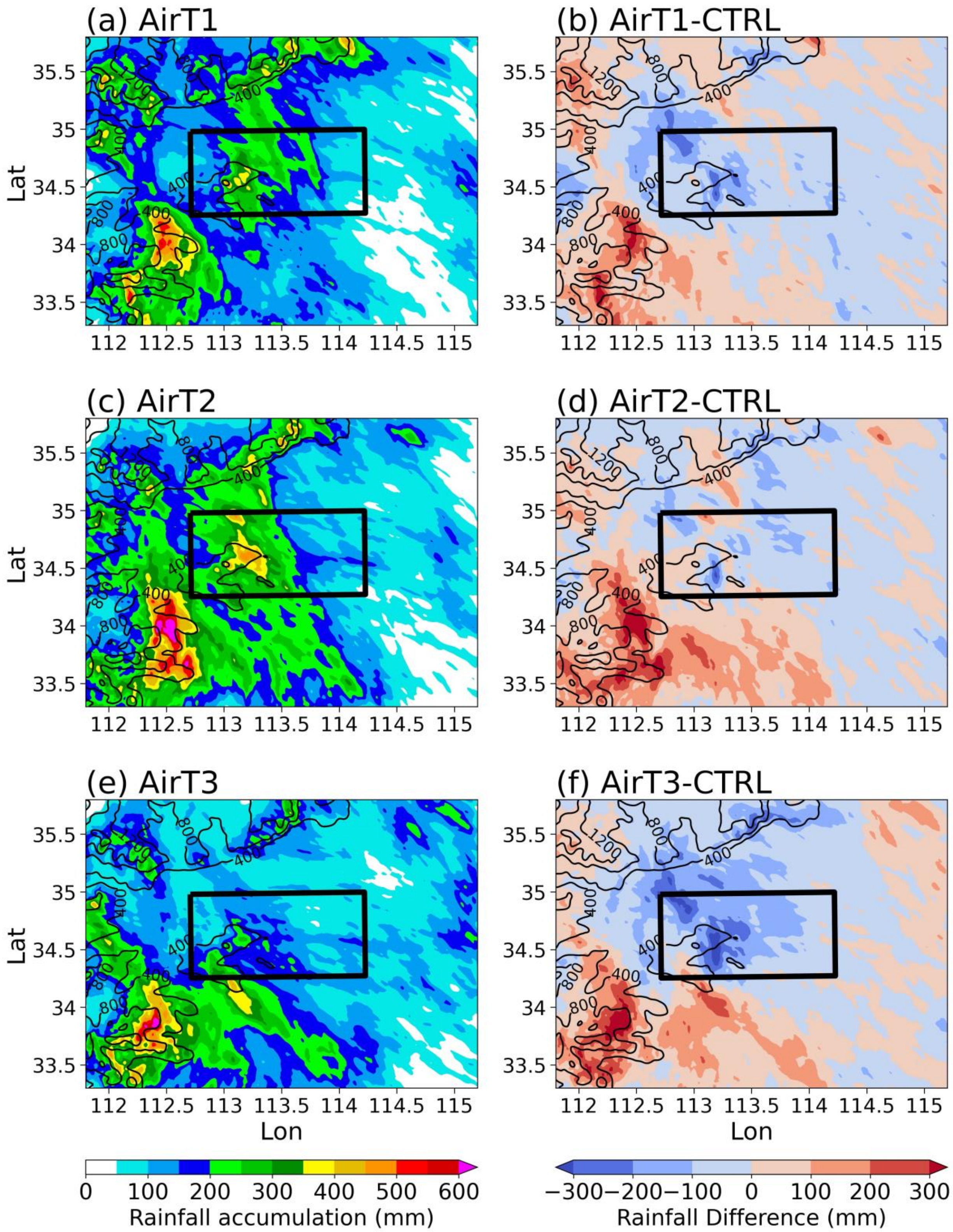

Figure 10. Spatial patterns of rainfall accumulation for three temperature-perturbation scenarios (a, c, e) and their difference from the CTRL simulation (b, d, f) during the period 06 UTC 19 July - 00 UTC 21 July 2021. The black box represents the Zhengzhou city. The contours represent the topography with an interval of 400 meters.

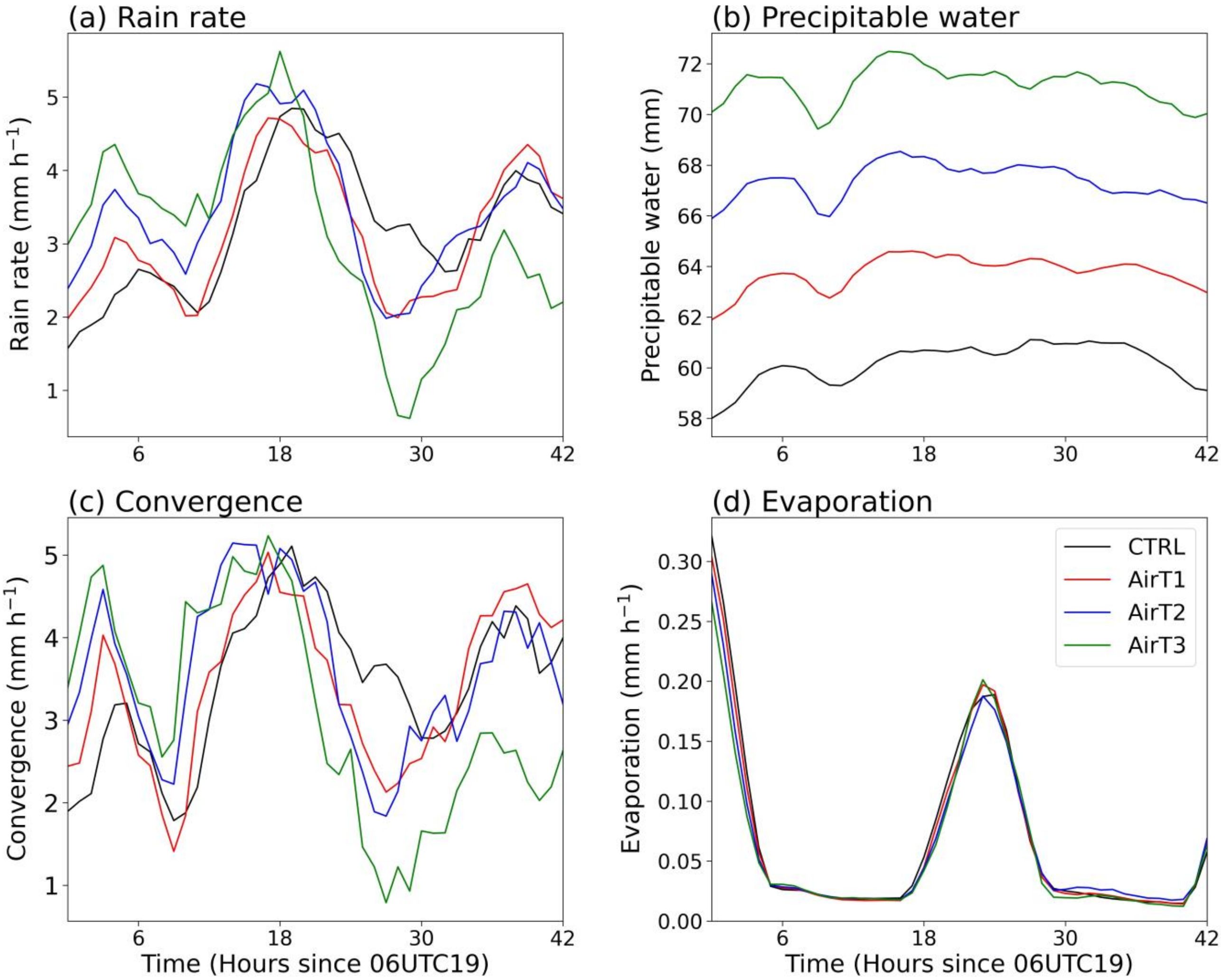

Figure 11. Time series of domain-average (a) rain rate (in mm h^{-1}), (b) precipitable water (in mm), (c) convergence of water vapor (in mm h^{-1}), and (d) evaporation rate (in mm h^{-1}) for the CTRL simulation and three temperature-perturbation scenarios.

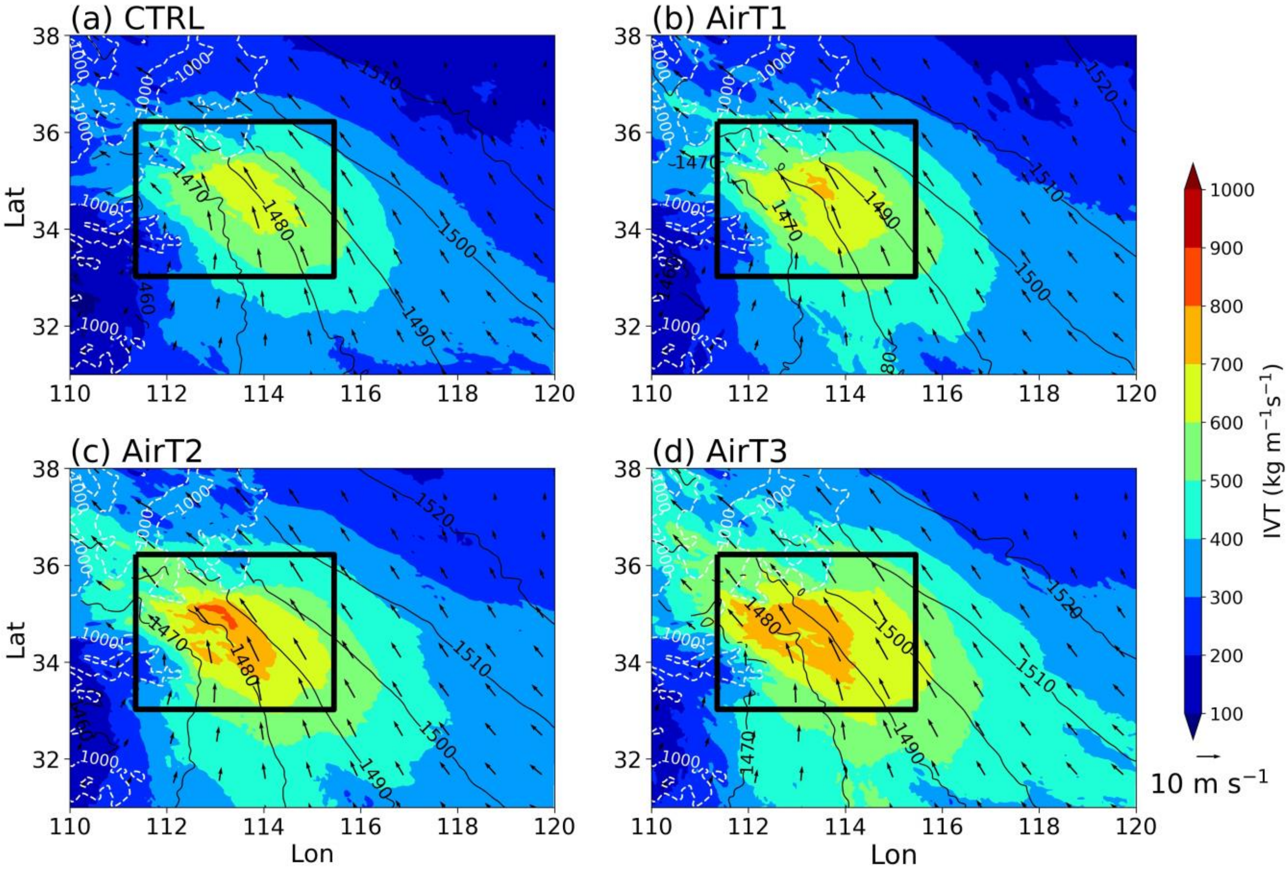

Figure 12. The spatial pattern of time-average integrated water vapor transport (shaded, in kg m^{-1} s^{-1}) during the study period for the (a) CTRL, (b) AirT1, (c) AirT2, and (d) AirT3 simulation. The contours show the time-average geopotential height at 850 hPa (in geopotential meters), while the vectors represent mean steering-level wind at 700 hPa (in m s^{-1}). The black box shows the boundary of domain 3. The white dashed contours show the topography with an interval of 800 meters.

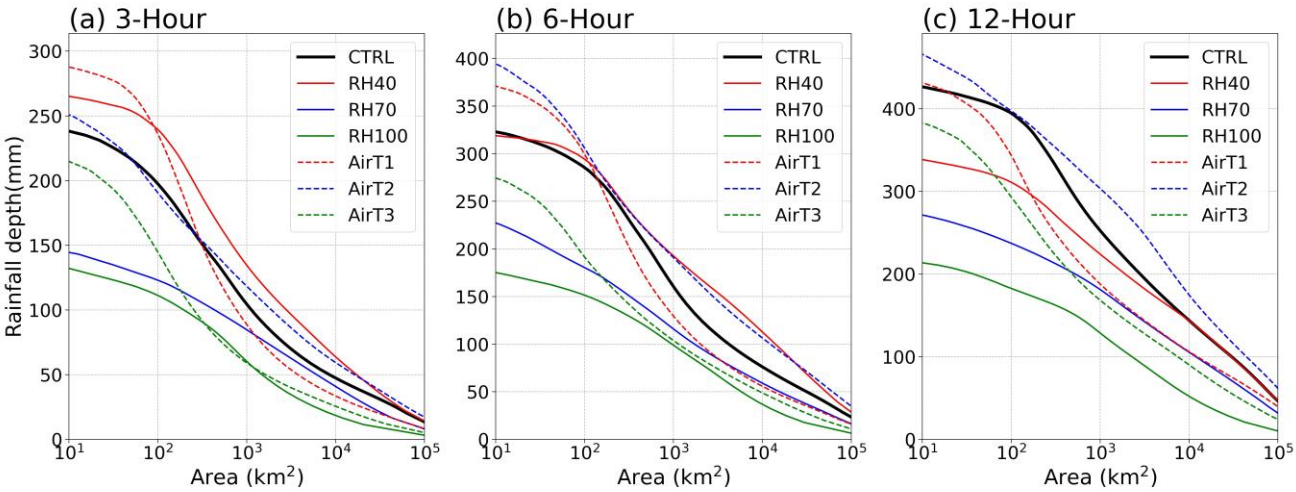

Figure 13. DAD curves derived from the CTRL simulation and different moisture/temperature perturbation scenarios. (a) 3 hours, (b) 6 hours, and (c) 12 hours.

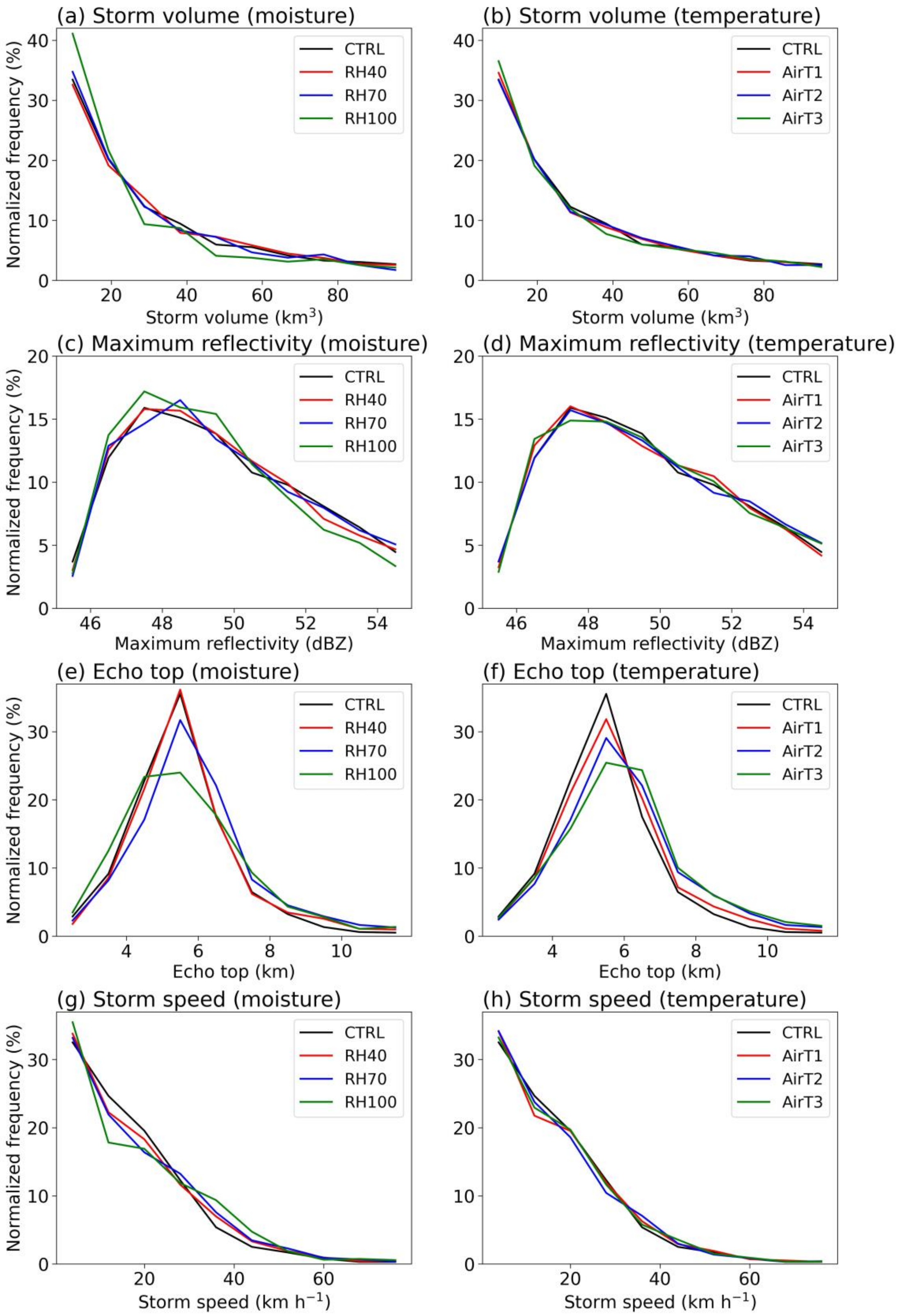

Figure 14. Distributions of storm properties derived from different moisture-perturbation scenarios (left column) and temperature-perturbation scenarios (right column). (a, b) storm cell volume (in km^3), (c, d) maximum reflectivity (in dBZ), (e, f) echo top height (in km), and (g, h) storm speed (in km h^{-1}).